Dipartimento di Fisica

CORSO DI LAUREA MAGISTRALE

INTERATENEO IN FISICA

Curriculum Fisica Nucleare e Subnucleare

TESI DI LAUREA MAGISTRALE

Muon track identification in the MUonE experiment at CERN

Laureanda:
Susanna Comunello

Relatore:
Prof. Giovanni Cantatore

ANNO ACCADEMICO 2024-2025

UNIVERSITÀ
DEGLI STUDI
DI TRIESTE

Dipartimento di Fisica

CORSO DI LAUREA MAGISTRALE

INTERATENEO IN FISICA

Curriculum Fisica Nucleare e Subnucleare

TESI DI LAUREA MAGISTRALE

Identificazione di tracce muoniche per l'esperimento MUonE del CERN

Laureanda:
Susanna Comunello

Relatore:
Prof. Giovanni Cantatore

ANNO ACCADEMICO 2024-2025

Abstract

The MUonE experiment aims at a precision independent determination of the leading–order hadronic vacuum-polarization contribution to the muon anomalous magnetic moment through a complementary, space-like approach. The method relies on measuring the running of the electromagnetic coupling at low negative momentum transfer by reconstructing with high precision the shape of the μ–e elastic scattering differential cross section. MUonE uses the 160 GeV muon beam at CERN and consists, in its final form, of a string of up to 40 independent tracking stations, each equipped with a thin low-Z target followed by an electromagnetic calorimeter and a "Muon Filter".

This thesis focuses on the reconstruction of muon tracks using the Muon Filter, a tracking station without target placed downstream of the electromagnetic calorimeter and conceived to identify muon tracks while suppressing other backgrounds. The analysis of the data from the 2025 test run at CERN demonstrates the essential role of this system for accurate particle identification, particularly in the small-angle scattering region where kinematic ambiguities are prevalent.

Sommario

L'obbiettivo dell'esperimento MUonE al CERN è una misura precisa e indipendente del contributo adronico dominante al momento magnetico del muone utilizzando un metodo sperimentale di nuova concezione. Esso è basato sulla misura dell'accoppiamento elettromagnetico a basso impulso trasferito nella determinazione di precisione della sezione d'urto differenziale della diffusione elastica μ–e. MUonE utilizza il fascio di muoni da 160 GeV disponibile al CERN e il suo apparato consiste, nella sua forma finale, di una successione di stazioni traccianti modulari e indipendenti, fino a 40 unità, ciascuna dotata di un bersaglio sottile a basso Z, seguita da un calorimetro elettromagnetico e da una stazione finale, priva di bersaglio, denominata "Muon Filter", concepita per identificare le tracce dei muoni sopprimendo i possibili fondi. Questa tesi si concentra sulla ricostruzione delle tracce muoniche ottenuta utilizzando il Muon Filter. L'analisi dei dati ottenuti nel "test run" del 2025 condotto al CERN dimostra il ruolo essenziale del Muon Filter nell'identificazione delle tracce, specialmente nella zona dei piccolli angoli di diffusione, dove i vincoli cinematici non sono sufficienti a discriminare le tracce elettroniche da quelle muoniche.

Contents

Introduction **11**

1 The anomalous magnetic moment of the muon **13**
1.1 Magnetic moments . . . 13
1.2 Electron anomalous magnetic moment . . . 15
1.3 Renormalization and running of α . . . 16
1.4 Muon anomalous magnetic moment . . . 17
1.4.1 QED contribution . . . 18
1.4.2 Electroweak contribution . . . 19
1.4.3 Hadronic contribution . . . 20
1.5 Theory vs. experiment . . . 24

2 The MUonE experiment **27**
2.1 Space-like approach to a_μ^{HLO} . . . 27
2.2 Experimental proposal . . . 29
2.3 $\mu - e$ scattering process . . . 30
2.3.1 Higher order corrections . . . 34
2.4 Sensitivity to $\Delta\alpha_{\text{had}}$ . . . 35
2.5 Tracking system . . . 37
2.5.1 Holographic Alignment Monitor . . . 40
2.6 Electromagnetic calorimeter . . . 41
2.7 Muon filter . . . 42
2.8 DAQ system . . . 43

3 Simulation framework and event reconstruction **47**
3.1 Simulation . . . 47
3.2 Track reconstruction . . . 48
3.3 Vertex reconstruction . . . 49
3.4 Muon track identification . . . 51
3.5 Kalman filter performance . . . 52

4 2025 Test run **55**

5 Conclusions **61**

Appendices **63**

A Kalman filter **63**

B Scattering angles distributions **67**

B.1 Simulation results 69

Bibliography **75**

Introduction

The muon anomalous magnetic moment, $a_\mu = (g_\mu - 2)/2$, is among the most precisely measured and computed observables in the Standard Model, at sub-ppm accuracy. The BNL E821 experiment first highlighted a tension with the then-current SM prediction, motivating a decade-long global effort to improve both experiment and theory. Fermilab's E989 collaboration has now delivered its final result using Runs 1–6, $a_\mu = 116\,592\,070.5(14.8) \times 10^{-11}$ (127ppb). Combined with BNL, the experimental world average is $a_\mu^{exp} = 116\,592\,071.5(14.5) \times 10^{-11}$ (124ppb). On the theory side, the 2025 update of the Muon g-2 Theory Initiative [1], which adopts a lattice QCD average for the leading order hadronic vacuum polarization (HVP) contribution to the muon gyromagnetic anomaly and combines it with standard QED, electroweak, and HLbL contributions, recommends $a_\mu^{SM} = 116\,592\,033(62) \times 10^{-11}$.

The MUonE experiment proposes an independent, complementary determination of the hadronic leading-order contribution a_μ^{HLO} by directly measuring the hadronic part of the running of the electromagnetic coupling $\Delta\alpha_{had}(t)$ in the space-like region at low momentum transfer via precision elastic scattering $\mu^\pm e^- \to \mu^\pm e^-$ [2]. In the space-like domain the relevant integrand is smooth and free of time-like resonances, which improves numerical stability and changes the systematic landscape compared with dispersive approaches based on $e^+e^- \to$ hadrons.

The full MUonE experimental apparatus consists of a sequence of 40 identical tracking stations, followed by an Electromagnetic CALorimeter (ECAL) and a Muon Filter (MF). Each station houses a structure, called "gondola", supporting a thin low-Z target and six tracking detector modules, for a total lever arm of ~ 1 m and transverse dimensions of $\sim 10 \times 10$ cm^2.

Many design choices have been made to reach the precision needed to determine the hadronic contribution at sub-percent level. A large number of stations reduces the statistical uncertainty on the scattering angle, while segmentation into many thin targets suppresses multiple Coulomb scattering. The tracking planes are tilted with respect to the beam to optimize acceptance and mitigate geometric biases. An active cooling system keeps temperature fluctuations below 2 K, and the mechanical structure is built in Invar to minimize thermal expansion. In addition to this, the relative spacing between the tracking planes must be stable with ≤ 10 µm accuracy. To monitor this requirement, a Holographic Alignment Monitor (HAM) system based on digital holographic interferometry has been developed.

Although the tracking system provides the main measurement of the outgoing muon and electron track angles, its discriminating power decreases in the region around 2–3 mrad. To solve this ambiguity, the apparatus relies on two Particle IDentification (PID) systems downstream of the tracking stations. The ECAL tags electrons and provides an independent measurement of their

energy, while the MF ensures efficient muon track identification at low scattering angles.
This thesis focuses on the reconstruction and identification of muon tracks using the Muon Filter. The work develops and assesses the downstream track–finding and fitting chain, the back-extrapolation to the upstream tracker and the quality criteria that turn these matches into a robust muon tag. The present study quantifies the matching efficiency, and evaluates how the MF information improves particle identification in the 2–3 mrad angular region where tracking alone is ambiguous.
Section 1 introduces the theory of the magnetic moment of the muon. Section 2 outlines the theoretical background of the MUonE experiment and describes the experimental apparatus. Section 3 presents the simulation and events reconstruction framework. Section 4 presents the analysis of the 2025 test run data.

1 The anomalous magnetic moment of the muon

1.1 Magnetic moments

In classical mechanics, the magnetic dipole moment $\vec{\mu}$ of a particle sets the torque it experiences in an external magnetic field $\vec{B}$. The associated potential energy and torque are

$$U = -\,\vec{\mu}\cdot\vec{B}, \qquad \vec{\tau} = \vec{\mu}\times\vec{B}. \tag{1.1}$$

For a particle of charge q and mass m moving on a circular orbit of radius r with speed v, the orbital motion produces a current

$$i = \frac{q}{T} = \frac{q}{2\pi r/v} = \frac{qv}{2\pi r}, \tag{1.2}$$

hence the orbital magnetic moment, with area $A = \pi r^2$, is

$$\vec{\mu}_{\rm orb} = i\,A\,\hat{\mathbf{n}} = \frac{qv}{2\pi r}\,\pi r^2\,\hat{\mathbf{n}} = \frac{qvr}{2}\,\hat{\mathbf{n}}, \tag{1.3}$$

where $\hat{\mathbf{n}}$ is normal to the orbital plane. The orbital angular momentum about the center is

$$\vec{L} = m\,\vec{r}\times\vec{v} = mvr\,\hat{\mathbf{n}}, \tag{1.4}$$

so that

$$\vec{\mu}_{\rm orb} = g_\ell\,\frac{q}{2m}\,\vec{L}, \qquad g_\ell = 1. \tag{1.5}$$

Beyond orbital motion, elementary particles carry an intrinsic angular momentum (spin) and an associated magnetic moment. For a spin-$\frac{1}{2}$ particle,

$$\vec{S} = \frac{\hbar}{2}\,\vec{\sigma}, \qquad \vec{\mu}_S = g_s\,\frac{q}{2m}\,\vec{S}. \tag{1.6}$$

For the electron ($q=-e$) one has $\vec{\mu}_S = -\,g_s\,\mu_B\,\vec{S}/\hbar$, where the Bohr magneton is $\mu_B \equiv e\hbar/(2m_e)$. Historically, the existence of an intrinsic moment was inferred from the anomalous Zeeman effect

and from space quantization (Stern–Gerlach). In 1925 Uhlenbeck and Goudsmit introduced electron spin to account for these observations [3]. The theoretical description of spin came in 1928 from Dirac's relativistic theory [4], which predicts $g_s = 2$ for a point-like spin-$\frac{1}{2}$ particle at tree level and, in the non-relativistic limit, leads to Pauli's equation

$$i\partial_0\psi = \Big[\frac{(\vec{p} - q\vec{A})^2}{2m} - \frac{q}{2m}\,\vec{\sigma}\cdot\vec{B} + qA_0\Big]\psi, \tag{1.7}$$

showing that one unit of spin couples twice as strongly to $\vec{B}$ as one unit of orbital angular momentum.

For nearly two decades after Dirac's prediction, measurements were consistent with $g = 2$. The picture changed in 1948, when Kusch and Foley, studying hyperfine splittings [5], reported the first clear deviation from the value predicted by Dirac, namely an electron magnetic anomaly

$$a_e = \frac{g_e - 2}{2} = 0.00119 \pm 0.00005. \tag{1.8}$$

Although Dirac's theory treats the electron as a point-like particle, so that in principle any deviation from $g = 2$ might suggest internal structure, the anomaly observed has a different explanation. As Schwinger showed in the same year [6], a structureless electron acquires an extra magnetic moment through its interaction with the quantized electromagnetic field. In quantum electrodynamics the physical electron is dressed by vacuum fluctuations, and the leading effect is the vertex correction illustrated in Fig. 1.1, where the electron couples to the external field while emitting and reabsorbing a virtual photon.

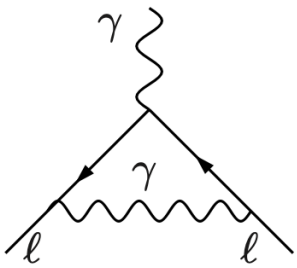

Figure 1.1: Lowest order QED contribution to the electron anomalous magnetic moment calculated by Schwinger.

Evaluating the one-loop diagram yields a universal shift of the magnetic form factor,

$$a_e = \frac{g_e - 2}{2} = \frac{\alpha}{2\pi} \simeq 0.00116, \tag{1.9}$$

where $\alpha = e^2/4\pi = 1/137$ is the fine structure constant, which means that g_e differs from 2 even for a point-like electron.
This result provided one of the earliest, decisive validations of Quantum Electrodynamics (QED) and of the renormalization program devised by Tomonaga, Schwinger, and Feynman to address the divergences arising in loop diagrams. Since then, a sustained theoretical effort has computed ever more precise contributions to the magnetic anomaly from all known particles and interactions, while experimental techniques have advanced significantly to measure these quantities with increasing accuracy. Nowadays, the electron and muon magnetic moments rank among the most precise measurements in physics and serve both as stringent tests of the Standard Model and as sensitive probes for potential new physics.

1.2 Electron anomalous magnetic moment

The electron anomalous magnetic moment provides one of the most stringent tests of QED. Within the Standard Model, non-QED effects, such as hadronic vacuum polarization, light-by-light scattering and electroweak loops, are strongly suppressed and enter only as small corrections. The QED part admits a perturbative expansion in powers of α/π, whose first term is the Schwinger result [7]:

$$a_e \equiv \frac{g_e - 2}{2} = \sum_{n \geq 1} C_n \left(\frac{\alpha}{\pi}\right)^n + a_e^{had+EW}, \qquad C_1 = \tfrac{1}{2}. \tag{1.10}$$

The expansion is known up to five loops, and the residual term a_e^{had+EW} accounts for hadronic and electroweak contributions, which are orders of magnitude smaller than the QED part.
On the experimental side, the Penning–trap determination of the electron g-factor [8] has reached the relative precision of 0.24 ppb (part-per-billion),

$$a_e^{exp} = 0.001\,159\,652\,180\,73(28), \tag{1.11}$$

which, when combined with the QED series (1.10), allows to extract the fine structure constant with exceptional accuracy. Equating theory and experiment, $a_e^{th} = a_e^{exp}$, one obtains

$$\alpha^{-1} = 137.035\,999\,149(33), \tag{1.12}$$

where the uncertainty is dominated by the experimental error on a_e and corresponds to a 0.24 ppb relative precision on α. This QED-based value can be compared with independent determinations of α that do not use a_e, such as atom–recoil measurements in matter–wave interferometers with rubidium [9] or cesium [10].

1.3 Renormalization and running of α

In QED, observables are computed perturbatively by expanding in powers of the electromagnetic coupling α and evaluating the corresponding Feynman diagrams. A central difficulty is the appearance of divergences: loop integrals run over virtual momenta that can reach arbitrarily large (ultraviolet) or small (infrared) scales. To handle them one first *regularizes* the theory (e.g. with a momentum cutoff Λ or dimensional regularization), and then *renormalizes* a finite set of parameters so that the divergent parts are absorbed into the bare quantities. This introduces a mass scale μ, the *renormalization scale*, which tracks how renormalized parameters depend on the energy at which the theory is probed. Since the vacuum is polarized by quantum fluctuations,

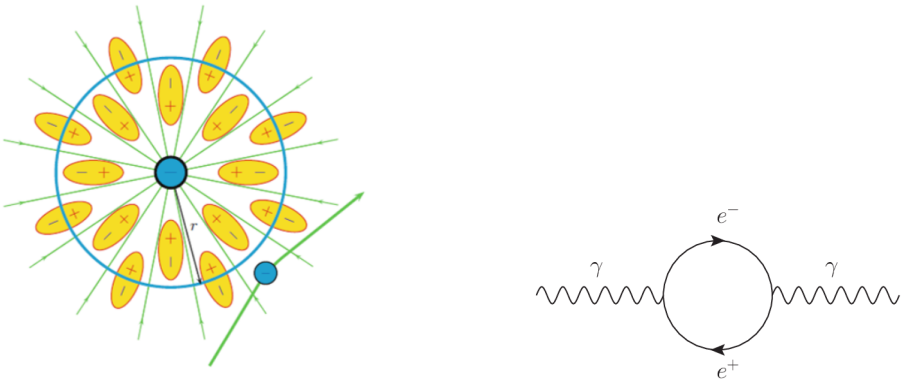

Figure 1.2: Representation of the vacuum polarization phenomenon causing charge screening by virtual pairs (left). Feynman diagram of the vacuum polarization effect (right).

an electron is surrounded by a cloud of virtual pairs (predominantly e^+e^-), as represented in Fig. 1.2. This screening makes measured quantities, such as the effective electric charge, depend on the probe's resolution: at higher momentum transfer q^2 (shorter distances), the probe penetrates the cloud more effectively and the electromagnetic interaction appears stronger. In other words,

the renormalized coupling "runs" with energy, while the bare parameters correspond to the unobservable values before vacuum effects.
The scale dependence is governed by the β function. At leading order in QED one finds

$$\beta(e) \equiv \frac{de}{d\ln\mu} = \frac{e^3}{12\pi^2}, \tag{1.13}$$

which implies, in terms of $\alpha \equiv e^2/(4\pi)$,

$$\frac{d\alpha}{d\ln\mu^2} = \frac{\alpha^2}{3\pi}. \tag{1.14}$$

Integrating between an arbitrary reference scale q_0 and q yields

$$\frac{1}{\alpha(q^2)} = \frac{1}{\alpha(q_0^2)} - \frac{1}{3\pi}\ln\left(\frac{q^2}{q_0^2}\right) \qquad \Longleftrightarrow \qquad \alpha(q^2) = \frac{\alpha(0)}{1-\Delta\alpha(q^2)}, \tag{1.15}$$

where $\alpha(0)$ is the fine-structure constant at zero momentum transfer and

$$\Delta\alpha(q^2) = \Delta\alpha_{lep}(q^2) + \Delta\alpha_{top}(q^2) + \Delta\alpha_{had}(q^2) \tag{1.16}$$

collects the vacuum polarization contributions of lepton, top-quark, and hadronic loops, respectively (the latter encoding non-perturbative QCD effects at low energies).
Vacuum polarization insertions modify the photon propagator and first enter lepton magnetic moments at $\mathcal{O}(\alpha^2)$. Since the momentum scales inside the loops depend on the lepton mass, these effects are the only source (at this order) of the difference between the electron and muon g-factors.

1.4 Muon anomalous magnetic moment

Whereas a_e is dominated by QED alone, the muon's larger mass ($m_\mu \simeq 206.77\, m_e$) enhances non-QED contributions with a characteristic m_ℓ^2 scaling. In practice, the electroweak, hadronic vacuum polarization (HVP) and hadronic light-by-light (HLbL) terms, which are negligible for the electron, become numerically relevant for the muon. As a result, a_μ is a precision interplay of QED, electroweak, and non-perturbative QCD, making it a sensitive probe of possible physics beyond the Standard Model.

The SM prediction for a_μ is generally divided into three parts

$$a_\mu^{SM} = a_\mu^{QED} + a_\mu^{EW} + a_\mu^{had}, \tag{1.17}$$

where a_μ^{QED} is known to five loops and sets the overall scale, a_μ^{EW} arises from $W^\pm$, Z, and H exchange, and the hadronic term dominates the theoretical uncertainty. The representative Feynman diagrams are shown in Fig. 1.3.

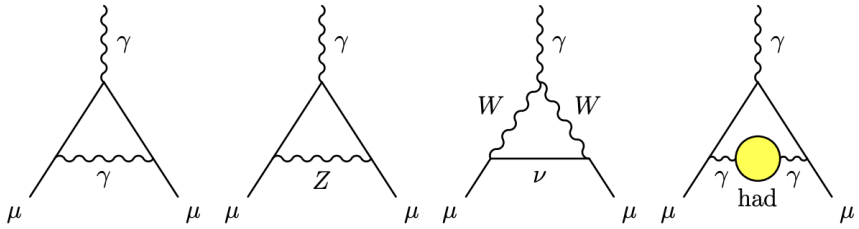

Figure 1.3: Diagrams which contribute to a_μ . From left to right: leading order QED (Schwinger term), lowest-order electroweak, lowest-order hadronic contribution.

The most recent calculation for the Standard Model value of a_μ is [1]:

$$a_\mu^{SM} = 116\,592\,033(62) \times 10^{-11} \tag{1.18}$$

In the following, the three contributions entering a_μ^{SM} are outlined: first the QED baseline and the electroweak correction, then the hadronic contribution with both the time-like dispersive evaluation and the space-like MUonE strategy.

1.4.1 QED contribution

The QED contribution to a_μ^{QED} can be divided according to the lepton-mass dependence as [1]

$$a_\mu^{QED} = A_1 + A_2(m_\mu/m_e) + A_2(m_\mu/m_\tau) + A_3(m_\mu/m_e, m_\mu/m_\tau), \tag{1.19}$$

where the first term is universal for all leptons and its lowest order contribution represents the one loop calculation given by Schwinger and shown in Fig. 1.1.
Each coefficient A_i can be expressed in the perturbation series of the fine structure constant,

analogously to what was done for the electron anomaly, as

$$A_i = \sum_{n=1,2,\cdots} \left(\frac{\alpha}{\pi}\right)^n A_i^{(2n)}. \tag{1.20}$$

Summing the terms in the perturbative QED expansion up to fifth order in α and using the measurement of α from Cs [10] and Rb [9] atoms oscillations, the value estimated in [1] is

$$a_\mu^{QED} = 116\,584\,718.8(2) \times 10^{-11}. \tag{1.21}$$

1.4.2 Electroweak contribution

By definition, the electroweak contribution to a_μ collects all SM terms that are not part of the pure QED, HVP, or HLbL parts. EW effects are mediated by the exchange of the heavy weak gauge bosons $W^\pm$, Z, and by the Higgs boson (see Fig. 1.4).

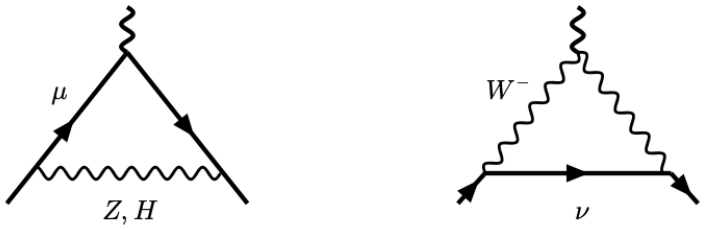

Figure 1.4: One-loop Feynman diagrams contributing to a_μ^{EW}.

At one loop the EW contribution scales as m_μ^2/M_W^2 and, in compact form, reads

$$a_\mu^{EW(1)} = \frac{5}{3}\frac{G_F\, m_\mu^2}{8\sqrt{2}\,\pi^2} \simeq 194.79(1) \times 10^{-11}, \tag{1.22}$$

i.e. it is suppressed with respect to the QED part but non-negligible numerically. Two-loop EW contributions, which include non-perturbative hadronic corrections, represent the main source of uncertainty. The resulting value of the electroweak contribution a_μ^{EW} is [1]

$$a_\mu^{EW} = 154.4(4) \times 10^{-11}. \tag{1.23}$$

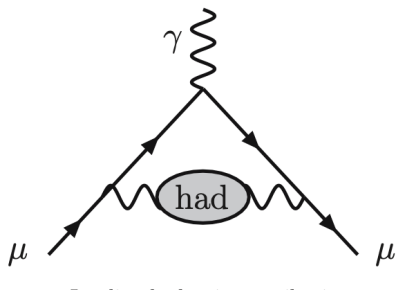

Figure 1.5: Hadronic leading order contribution to the muon anomaly.

1.4.3 Hadronic contribution

Hadronic effects dominate the theoretical uncertainty because their evaluation involves non-perturbative QCD at low energies, where fixed-order perturbation theory is not applicable. The hadronic contribution can be divided in three parts, regarding the leading and next to leading order Vacuum Polarization (VP) effects, respectively a^{HLO} and a^{HNLO}, and the light-by-light contribution a^{HLbL}

$$a_\mu^{had} = a^{HLO} + a^{HNLO} + a^{HLbL}. \tag{1.24}$$

The leading hadronic contribution $O(\alpha^2)$ comes from vacuum polarization diagrams, like the one shown in Fig. 1.5. The addition of another vacuum polarization loop, being both leptonic or hadronic, contributes to the next to leading order effect.
Given the difficulties associated to QCD direct calculations, HLO contribution to a_μ can be evaluated with the so-called time-like approach, which makes use of causality and unitarity as main principles, integrating the experimentally obtained electron-positron annihilation data measured in a time-like region.
Due to the analiticity of the vacuum polarization function, the following dispersion relation holds

$$\frac{\Pi_\gamma^{had}}{q^2} = \int_0^\infty \frac{ds}{s}\,\frac{1}{\pi}\,\mathrm{Im}\Pi_\gamma^{had}(s)\,\frac{1}{q^2 - s}, \tag{1.25}$$

representing the hadronic VP contribution.

The optical theorem enables one to relate the imaginary part of the vacuum polarization ampli-

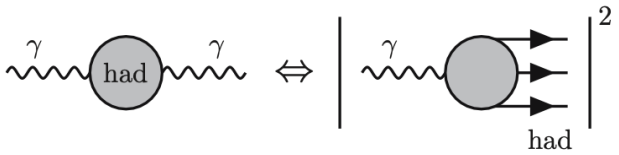

Figure 1.6: Schematic representation of the optical theorem.

tude to the total cross section of the time-like process $e^+e^- \to$ hadrons (Fig. 1.6)

$$\mathrm{Im}\Pi_\gamma^{had}(s) = \frac{s}{4\pi\alpha}\,\sigma^0_{had}(e^+e^- \to had) = \frac{\alpha}{3}\,R_{had}(s), \tag{1.26}$$

where the R-ratio

$$R_{had}(s) = \frac{\sigma^0_{had}}{4\pi\alpha^2/(3s)} \tag{1.27}$$

depends on the measured cross section.
Eq. 1.25 requires the bare cross section for e^+e^- annichilation rather than the measured one. The bare quantity can be expressed in terms of the measurable one as

$$\sigma^0_{had} = \sigma_{had}\frac{\alpha^2}{\alpha(s)^2}. \tag{1.28}$$

The R-ratio then becomes

$$R_{had}(s) = \frac{\sigma_{had}}{4\pi\alpha(s)^2/(3s)} \tag{1.29}$$

Exploiting the dispersion relation Eq. 1.25, the lowest order hadronic contribution to the anomaly can be computed through [11]

$$a_\mu^{HLO} = \frac{\alpha}{\pi^2}\int_0^\infty ds\;\mathrm{Im}\Pi_{had}(s)\;\frac{K(s)}{s}, \tag{1.30}$$

where $\Pi_{had}(s)$ is the hadronic part of the photon vacuum polarization,

$$K(s) = \int_0^1 dx\;\frac{x^2(1-x)}{x^2(1-x)(s/m_\mu^2)} \tag{1.31}$$

is a positive kernel function and m_μ is the muon mass.
It is convenient to separate the integral into a low-energy contribution and a high-energy tail

$$a_\mu^{HLO} = \left(\frac{\alpha m_\mu}{3\pi}\right)^2 \left[\int_0^{E_{cut}^2} ds\, \frac{R_{had}^{data}(s)\hat{K}(s)}{s^2} + \int_{E_{cut}^2}^{\infty} ds\, \frac{R_{had}^{pQCD}(s)\hat{K}(s)}{s^2}\right], \tag{1.32}$$

where E_{cut} is the energy up to which the data must be used and from where it is safe to use the perturbative QCD (pQCD), and

$$\hat{K}(s) = \frac{3s}{m_\mu^2} K(s) \tag{1.33}$$

is the rescaled kernel function.

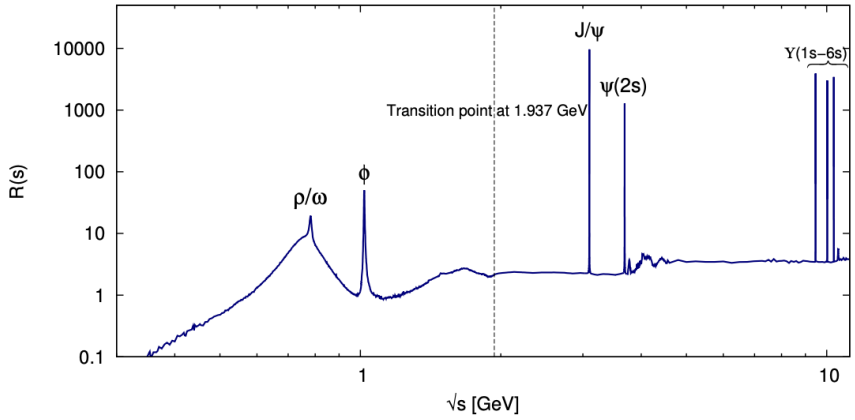

Figure 1.7: Hadronic R-ratio shown in the range $m_\pi \leq \sqrt{s} \leq 1.937$ GeV. The dashed line marks the transition point where evaluations switch from a sum over exclusive channels to inclusive *R(s)* data [12].

In Fig. 1.7 and the behavior of the $R(s)$ ratio is shown as a function of $\sqrt{s}$. At low energies the spectrum is dominated by vector–meson resonances (ρ, ω, ϕ, $\cdots$), so a perturbative treatment is not applicable. The biggest contribution ($\sim 75\%$) is the ρ at ~ 0.77 GeV, which drives the main channel $e^+e^- \to \pi^+\pi^-$. With increasing energy, more channels open up, and the evaluation becomes harder. Only beyond a few GeV $R(s)$ evolves toward the smoother continuum where pQCD provides a reliable description. Fig. 1.8 shows the contributions of all possible different final states to the whole value of *R(s)*.
The dispersive, time-like determination of a_μ^{HLO} requires combining together many $e^+e^- \to$ hadron measurements over different energy intervals. This is intrinsically delicate: statistical

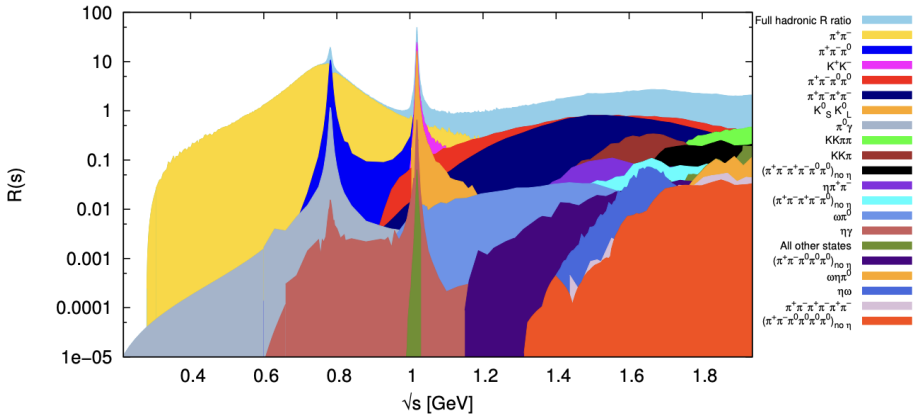

Figure 1.8: The hadronic $R(s)$-ratio.

errors are usually treated as gaussian and combined in quadrature, but systematic uncertainties depend on each machine and detector, can change with running conditions, and are often correlated across energy points. Even within a single experiment, scans taken at different times may require careful treatment of evolving detector conditions and normalization. A major advance was the use of initial state radiation (ISR) method, pioneered by KLOE [13], which records events with a hard photon emitted by the initial state so that a broad range of effective $\sqrt{s'}$ is covered while the collider runs at fixed $\sqrt{s}$. Working at a single beam energy keeps detector conditions uniform and reduces machine related systematics [14].

Even after combining datasets, several analysis choices remain non-unique, including the interpolation and modeling of $R(s)$ between points, the treatment of correlations, the definition of the energy integral, and the threshold for switching to theory input.

The most precise measurement of the $\pi^+\pi^-$ cross section for BABAR [15], KLOE [16] and, recently, CMD-3 [17] experiments do not agree within the given uncertainties, as shown in Fig. 1.9.

The Muon $g-2$ Theory Initiative White Paper [1] recommended an estimate of $a_\mu^{HLO} = 704.5(6.1) \times 10^{-10}$, where the final error is evaluated taking into account the tension between different experimental results. Including higher-order vacuum polarization terms, the final VP contribution results in

$$\begin{aligned} a_\mu^{HVP} &= a_\mu^{HLO} + a_\mu^{HNLO} + a_\mu^{HNNLO} \\ &= [704.5(6.1) - 9.83(0.07) + 1.24(0.01)] \times 10^{-10} \\ &= 695.9(6.1) \times 10^{-10}. \end{aligned} \tag{1.34}$$

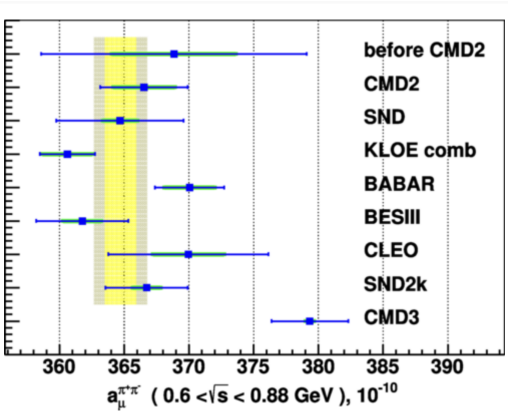

Figure 1.9: $\pi^+\pi^-$ contribution to a_μ^{HLO} from the energy range $0.6 < \sqrt{s} < 0.88$ GeV for different experiments. The yellow band corresponds to the average of all experiments before CMD-3, where the gray band includes additional uncertainty inflation due to the KLOE/BABAR inconsistency [17].

1.5 Theory vs. experiment

As discussed above, the muon anomaly receives contributions from QED, electroweak, and hadronic effects,

$$a_\mu^{SM} = a_\mu^{QED} + a_\mu^{EW} + a_\mu^{HAD}, \tag{1.35}$$

where the hadronic term includes the leading and higher order vacuum polarization (HVP) contributions and the hadronic light–by–light (HLbL) contribution. The present SM reference (WP25) [1], which adopts a lattice QCD average for the LO HVP and combines it with standard QED, EW, and HLbL inputs, yields

$$a_\mu^{SM} = 116\,592\,033(62) \times 10^{-11}. \tag{1.36}$$

This can be compared with the current experimental average,

$$a_\mu^{exp} = 116\,592\,071.5(14.5) \times 10^{-11}, \tag{1.37}$$

so that, at the present level of precision:

$$\Delta a_\mu \equiv a_\mu^{exp} - a_\mu^{SM} = 38(63) \times 10^{-11}. \tag{1.38}$$

Still, the discrepancy between the data-driven calculation and the lattice approach must be resolved by the theory, also in light of the unexplained tension between the bulk of experimental e^+e^- measurements and the outlier represented by the CMD-3 results, as seen in Fig. 1.9.

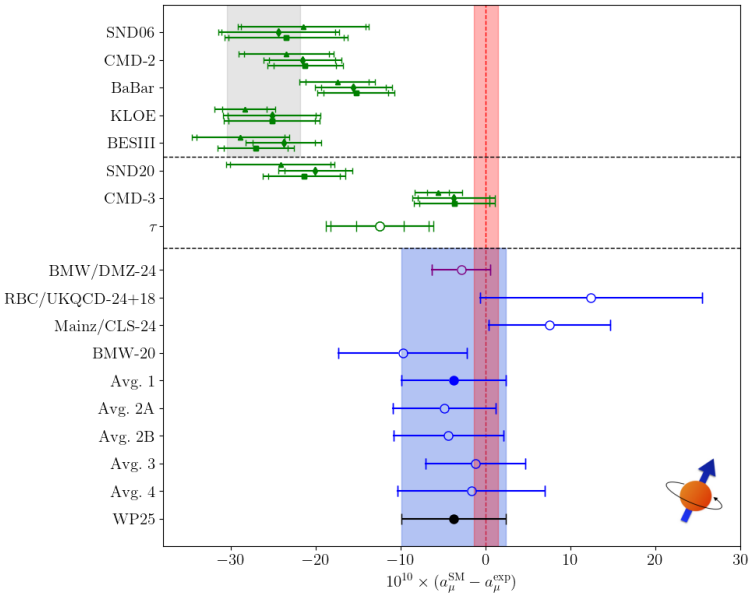

Figure 1.10: Summary of the current SM prediction for a_μ compared to the experimental average (red band and points). The WP25 prediction is shown in black and as the blue band, derived from the lattice QCD LO HVP "Avg. 1" (blue points). The gray band indicates the WP20 result [18], based on e^+e^- data (green points).

Looking ahead, the SM uncertainty must be reduced by roughly a factor of four to match the precision of the current experimental average after the final result from the E989 experiment at Fermilab. A key priority is resolving tensions among data–driven HVP evaluations with new $e^+e^- \to$ hadrons measurements, improved theory inputs (including event generators and isospin–breaking corrections), and updated τ data from Belle II. Complementary approaches with different systematics are equally important: the MUonE space–like program will measure $\Delta\alpha_{had}(t)$ directly, and the E34 experiment at J–PARC [19] will provide an independent determination of a_μ. The combined progress of these efforts, together with continued advances in lattice QCD and new time–like data, offers the most robust path to a SM prediction commensurate

with the experimental accuracy and, if a residual difference remains, to a clearer assessment of possible physics beyond the Standard Model.

2 The MUonE experiment

The MUonE experiment aims to provide an independent and precise determination of the leading–order Hadronic Vacuum–Polarization (HVP) contribution to the muon anomalous magnetic moment. Unlike time–like, data–driven dispersive evaluations, MUonE exploits the space–like running of the electromagnetic coupling by measuring with high accuracy the differential cross section of elastic muon-electron scattering [2].
To achieve the required precision, it is essential to measure both the direction and the momentum of the incoming muons, as well as the direction of the outgoing particles. The CERN M2 muon beam, operated at 160 GeV with an average intensity of about 1.3×10^7 muons per second, provides the necessary conditions for this measurement [20].

2.1 Space-like approach to a_μ^{HLO}

The MUonE experiment aims at determining a_μ^{HLO} using a new method, based on the direct measurement of $\Delta\alpha_{had}$ in the space-like region [21]. The leading-order hadronic contribution to the muon g-2 in the time-like approach is given by Eq. 1.30. Exchanging the integration order between x and s, one gets

$$a_\mu^{HLO} = \int_0^1 dx\ m_\mu^2 x^2 \int_0^\infty \frac{ds}{s} \frac{\mathrm{Im}\Pi_{had}(s)}{\frac{x^2 m_\mu^2}{1-x} + s}. \tag{2.1}$$

The integral over the s variable can be simplified using the following dispersion relation for the vacuum polarization

$$\overline{\Pi}_{had}(t) = \Pi_{had}(t) - \Pi_{had}(0) = \frac{t}{\pi} \int_0^\infty \frac{ds}{s}\ \frac{\mathrm{Im}\Pi_{had}(s)}{t - s}, \tag{2.2}$$

leading to

$$a_\mu^{HLO} = \frac{\alpha}{\pi^2} \int_0^1 dx\ (x-1)\ \overline{\Pi}_{had}[t(x)], \tag{2.3}$$

where

$$t(x) = \frac{x^2 m_\mu^2}{x-1} < 0 \tag{2.4}$$

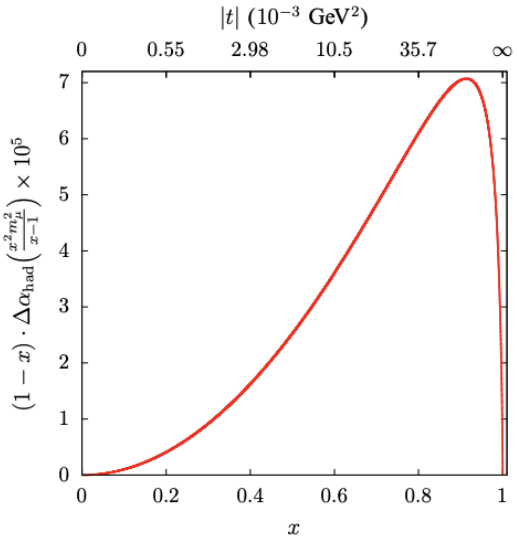

Figure 2.1: Integrand $(1-x)\Delta\alpha_{had}[t(x)]$ as a function of t and x [23].

is the space-like four-momentum transfer.

The running of the electromagnetic coupling constant is linked to the photon vacuum polarization function by the relation

$$\Delta\alpha(q^2) = -\mathrm{Re}\overline{\Pi}(q^2). \tag{2.5}$$

Since $\mathrm{Im}\Pi(q^2) = 0$ for $q^2 = t < 0$, Eq. 2.3 becomes [22]

$$a_\mu^{HLO} = \frac{\alpha}{\pi}\int_0^1 dx\ (1-x)\Delta\alpha_{had}[t(x)], \tag{2.6}$$

This formula enables the determination of the leading hadronic vacuum-polarization contribution to the muon anomaly from the space-like measurement of $\Delta\alpha_{had}(t)$.

Unlike the time-like dispersive relation in Eq. 1.30, which depends on $R_{had}^{data}(s)$, and inherits its resonant fluctuations, the integrand here is smooth and resonance-free, as illustrated in Fig. 2.1. The peak occurs at $x_{peak} = 0.914$, corresponding to $t = -0.108$ GeV^2, and $\Delta\alpha_{had}(t_{peak}) \simeq 7.86 \times 10^{-4}$.

A further advantage is that the running of α in the region of interest for the evaluation of a_μ^{HLO} can be measured by a single scattering experiment. Thus, the space-like approach is not affected by the systematic uncertainties due to handling data from different experiments, which is the

main limitation of the time-like method.
This space-like dispersive approach forms the foundation of the MUonE project and will be outlined in the next section.

2.2 Experimental proposal

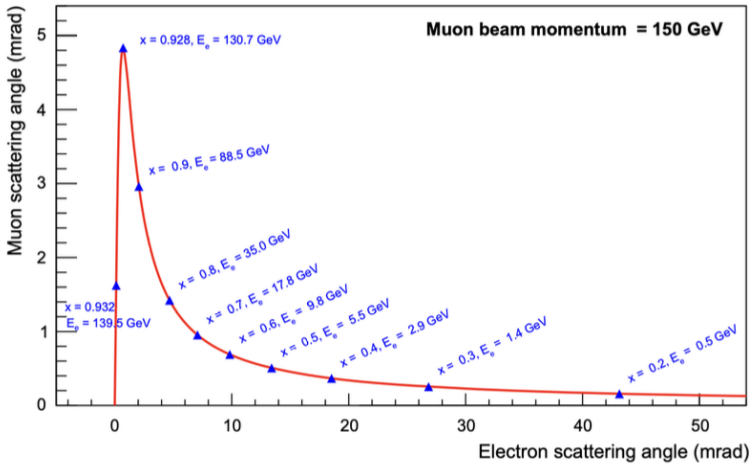

Figure 2.2: Relation between the muon and electron scattering angles for a 150 GeV incident muon beam.

The MUonE experiment aims to extract $\Delta\alpha_{had}$ from the measurement of the differential cross section of the $\mu^{\pm}e^{-} \to \mu^{\pm}e^{-}$ elastic scattering. It is performed by scattering a muon beam of E_{μ} = 160 GeV, available at the CERN M2 beamline [20], on the atomic electrons of a fixed low-Z target. The reasons for which the proposed tecnique is appealing are the following [23]:

- the $\mu - e$ scattering is a pure t-channel process where the dependence on t of the differential cross section is proportional to $|\alpha(t)/\alpha(0)|^2$

$$\frac{d\sigma}{dt} = \frac{d\sigma_0}{dt}\left|\frac{\alpha(t)}{\alpha(0)}\right|^2, \tag{2.7}$$

  where $d\sigma_0/dt$ is the effective Born cross section;

- the highly energetic muons from the beam allow to access the region of the peak of the integrand function in Eq. 2.6 (see Fig. 2.1);

- the highly boosted kinematics allows to cover the whole acceptance with a single and homogeneous detector: the angular deflections will be contained within a cone of 50 mrad;

- the kinematics of the elastic scattering is completely determined by the angular observables; this allows to identify the signal region through the correlation of muon and electron scattering angles as shown in Fig. 2.2.

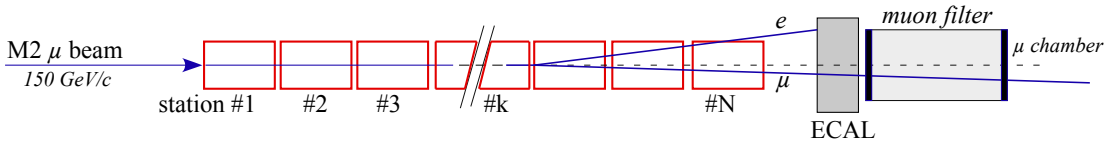

Figure 2.3: Schematic representation of the MUonE apparatus.

The full experimental apparatus [2] consists of a sequence of 40 identical, yet independent, tracking stations, followed by an Electromagnetic CALorimeter (ECAL) and a Muon Filter (MF), as shown in Fig. 2.3.
Each station houses a structure, called "gondola", supporting a thin low-Z target made of beryllium (15 mm thickness) or graphite (10 mm thickness) and 6 tracking detector modules, for a total lever arm of ~ 1 m and transverse dimensions of $\sim 10 \times 10$ cm^2.

A detector area of this size fully contains the angular acceptance of interest, accommodating scattering angles up to about 30 mrad; at a beam momentum of 160 GeV, this corresponds to outgoing electrons with energies above roughly 1 GeV.
The target material and segmentation ensure that the total effective target thickness reaches the ~ 60 cm needed for sufficient statistics, while at the same time minimizing the impact of Multiple Coulomb Scattering (MCS) on the angular resolution.
Although the tracking system provides the main measurement of the outgoing muon and electron track angles, its discriminating power decreases in the region around 2–3 mrad. To solve this ambiguity, the apparatus relies on two Particle IDentification (PID) systems downstream of the tracking stations. The ECAL tags electrons and provides an independent measurement of their energy, while the MF ensures efficient muon track identification at low scattering angles.
Since the measurement is purely angular, the mapping from the observed angles to the momentum transfer t is presented next.

2.3 $\mu - e$ scattering process

At Born level the muon-electron elastic scattering (Fig. 2.4) is represented by the interaction

$$\mu^{\pm}(p_1)\, e^{-}(p_2) \to \mu^{\pm}(p_3)\, e^{-}(p_4), \tag{2.8}$$

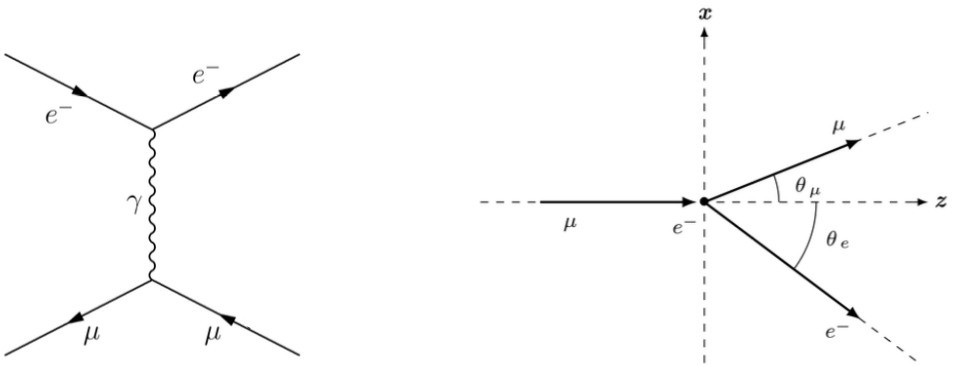

Figure 2.4: Feynman diagram for $\mu^{\pm}e$ elastic scattering (left); $\mu^{\pm}e$ elastic scattering in the laboratory reference frame (right).

where p_1, p_2 and p_3, p_4 are the four-momenta respectively of the initial and final state.
Fig. 2.4 gives a schematical representation of the process in the laboratory reference frame. The particle 4-momenta can be written as follows

$$\begin{aligned} p_1 &= (E_\mu,\ \vec{p}_\mu) = (E_\mu,\ 0,\ 0,\ p_\mu) \\ p_2 &= (E_e,\ \vec{p}_e) = (m_e,\ 0,\ 0,\ 0) \\ p_3 &= (E'_\mu, \vec{p}'_\mu) = (E'_\mu,\ p'_\mu \sin\theta_\mu,\ 0,\ p'_\mu \cos\theta_\mu) \\ p_4 &= (E'_e, \vec{p}'_e) = (E_e,\ p'_e \sin\theta_e,\ 0,\ p'_e \cos\theta_e) \end{aligned} \tag{2.9}$$

where p_μ is the incoming muon momentum, while $(E'_\mu, \vec{p}'_\mu)$ and $(E'_e, \vec{p}'_e)$ are the energies and momenta of the outgoing muon and electron respectively.
The differential cross section at leading order in QED is given by

$$\frac{d\sigma_0}{dt} = \frac{4\pi\alpha^2}{t^2 \lambda(s, m_e^2, m_\mu^2)} \left[(s - m_\mu^2 - m_e^2)^2 + st + \frac{t^2}{2} \right], \tag{2.10}$$

where s and t are the usual Mandelstam variables, and λ is the Källén function

$$\begin{aligned} s &= (p_1 + p_2)^2 = (p_3 + p_4)^2 = m_\mu^2 + m_e^2 + 2m_e E_\mu \\ t &= (p_1 - p_3)^2 = (p_2 - p_4)^2 = 2m_e(m_e - E_e) \\ \lambda(s, m_e^2, m_\mu^2) &= (s - m_\mu^2 - m_e^2)^2 - 4m_\mu m_e = 4m_e^2(E_\mu^2 - m_\mu^2). \end{aligned} \tag{2.11}$$

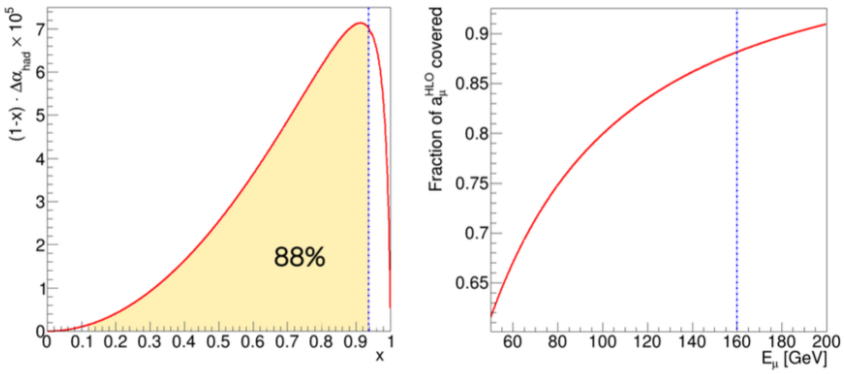

Figure 2.5: Coverage of a_μ^{HLO} for $E_\mu = 160$ GeV (left). Fraction of a_μ^{HLO} covered as a function of the muon beam energy (right).

For a fixed incoming muon momentum, the four-momentum transfer reaches a maximum at $q^2_{max} = -t_{min}$

$$t_{min} = -\frac{\lambda(s, m_e^2, m_\mu^2)}{s}. \tag{2.12}$$

The Lorentz parameters connecting the LAB and CM frames are

$$\begin{aligned} \gamma &= \frac{E_\mu + m_e}{\sqrt{s}} \\ \beta &= \frac{p_\mu}{E_\mu + m_e}, \end{aligned} \tag{2.13}$$

so that the corresponding CM energy is $\sqrt{s} \sim 0.405541$ GeV and $\gamma \sim 370$.
Using the CERN M2 beam at the reference energy $E_\mu = 160$ GeV allows to cover the momentum transfer region -0.153 GeV$^2 < t < 0$ GeV^2, which is equivalent to $0 < x < 0.936$ and corresponds to $\sim 88\%$ of the integrand in Eq. 2.6, as shown in Fig. 2.5 [24]. The remaining fraction can be computed by extrapolating $\Delta\alpha_{had}$ in the region kinematically not accessible to the experiment $0.936 < x < 1$, using an appropriate parameterization for the hadronic contribution to the vacuum polarization [25].
The correlation between the muon and electron scattered angles can be obtained from the transverse momentum conservation

$$\theta_\mu(\theta_e) = \arcsin\left[\frac{\sqrt{E_e^2(\theta_e) - m_e^2}}{[E_\mu + m_e - E_e(\theta_e)]^2 - m_\mu^2}\sin\theta_e\right], \tag{2.14}$$

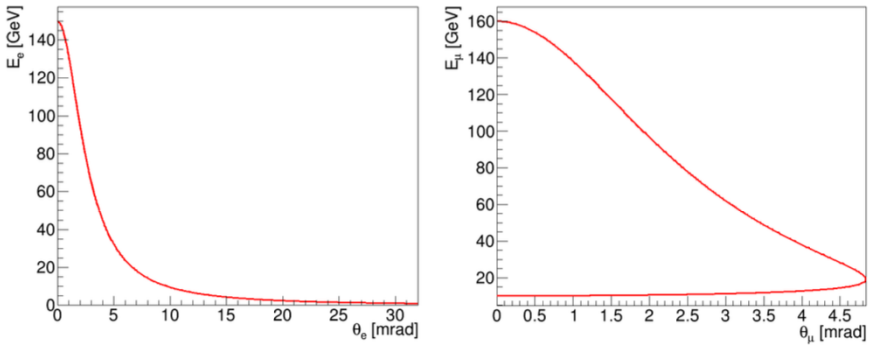

Figure 2.6: Outgoing electron energy as a function of its scattering angle (left).Outgoing muon energy as a function of its scattering angle (right).

where $E_e(\theta_e)$ is the final energy of the electron, given the reconstructed θ_e

$$E_e(\theta_e) = m_e \frac{1 + r^2 \cos^2\theta_e}{1 - r^2 \cos^2\theta_e} \qquad r = \frac{\sqrt{E_\mu^2 - m_\mu^2}}{E_\mu + m_e}. \tag{2.15}$$

The maximum energy value occurs at $\theta_e = 0$, and corresponds to $E_e^{max} \simeq 149.8$ GeV for the selected beam energy. A similar expression can be also derived for the outgoing muon energy as a function of θ_μ

$$E'_\mu(\theta_\mu) = \frac{a \pm b(\theta_\mu) p_\mu^2 \cos\theta_\mu}{d(\theta_\mu)}, \tag{2.16}$$

where

$$a = (E_\mu + m_e)(m_\mu^2 + m_e E_\mu) \tag{2.17}$$

$$b(\theta_\mu) = \sqrt{m_e^2 - m_\mu^2 \sin^2\theta_\mu} \tag{2.18}$$

$$d(\theta_\mu) = (E_\mu + m_e)^2 - p_\mu^2 \cos^2\theta_\mu. \tag{2.19}$$

Note that the muon energy is not uniquely determined by its scattering angle, contrarily to the electron case. The two functions are represented in Fig. 2.6.

It is also useful to obtain the differential cross section as a function of the two observed scattering

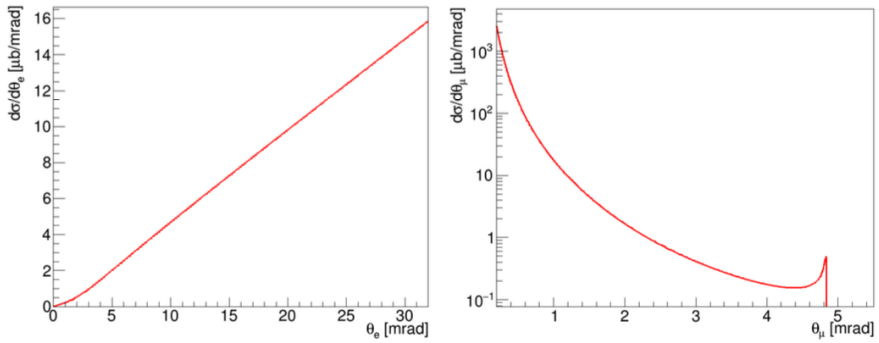

Figure 2.7: Differential cross section of the $\mu - e$ elastic scattering at LO, as a function of the electron scattering angle (left) and the muon scattering angle (right).

angles, by expressing the momentum transfer in terms of θ_e and θ_μ

$$t(\theta_e) = t_{ee} = \frac{4m_e^2 r^2 \cos^2\theta_e}{r^2\cos^2\theta_e - 1} \qquad t(\theta_\mu) = t_{\mu\mu} = 2m_e\left(\frac{a \pm b(\theta_\mu)p_\mu^2\cos^2\theta_\mu}{d(\theta_\mu)} - E_\mu\right) \tag{2.20}$$

and calculating the differential cross sections by means of a change of variable

$$\frac{d\sigma_0}{d\theta_e} = \frac{d\sigma_0}{dt}\left|\frac{dt}{d\theta_e}\right| \qquad \frac{d\sigma_0}{d\theta_\mu} = \frac{d\sigma_0}{dt}\left|\frac{dt}{d\theta_\mu}\right|. \tag{2.21}$$

The two differential cross sections are plotted in Fig. 2.7.

2.3.1 Higher order corrections

The LO QED prediction for the elastic differential cross section is not sufficient for the target 10 ppm experimental precision: NLO and NNLO corrections need to be taken into consideration. The complete theoretical cross section needed for the experiment can be expressed as the sum of the following terms

$$\begin{aligned}\sigma(\mu^\pm e^- \to \mu^\pm e^-) \approx LO(QED) \ &+ LO(EW) + \\ &+ NLO(QED) + NLO(HAD) + NLO(EW) + \\ &+ NNLO(QED) + NNLO(HAD) + NNLO(EW).\end{aligned} \tag{2.22}$$

Here, LO(QED) is the Born cross section of Eq. 2.10; NLO(QED) and NNLO(QED) are higher-order QED corrections. The electroweak term LO(EW), dominated by Z exchange, is small

but non-negligible, $\mathcal{O}(10^{-5})$ [26]; by contrast, NLO(EW) is highly suppressed with respect to NLO(QED) and can be safely neglected to speed up NLO Monte Carlo generation [25]. The hadronic piece of primary interest is NLO(HAD), i.e. the vacuum-polarization insertion in the photon propagator. The NNLO(HAD) correction, involving non-factorizable hadronic loops [27], is more intricate but still relevant at the $10^{-4} - 10^{-5}$ level.

Beyond LO, radiative effects differentiate μ^+e^- from μ^-e^- scattering, and the momentum transfers reconstructed from the electron and muon kinematics, t_{ee} and $t_{\mu\mu}$, no longer coincide due to real-photon emission $\mu^\pm e \to \mu^\pm e\gamma$. As shown in Fig. 2.8 [26], the QED NLO/LO ratio can exceed 10% at large $|t|$ without elasticity selections; although this is expected to be much smaller with standard elastic cuts, accurate NLO control remains essential.

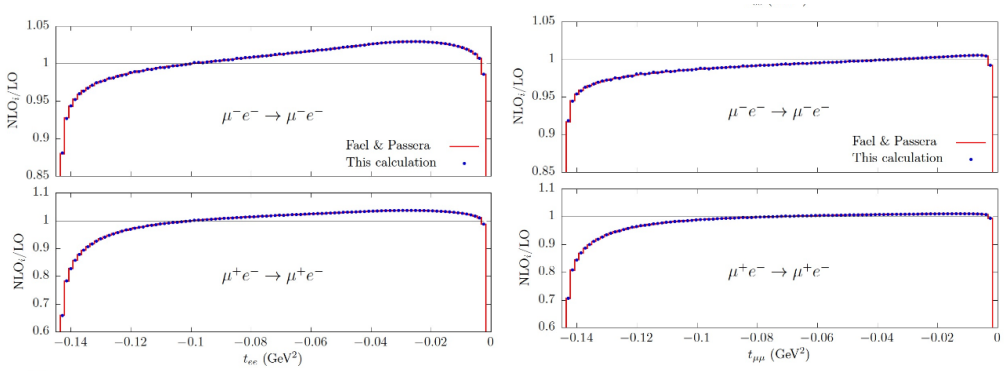

Figure 2.8: Ratio of the NLO and LO cross section as a function of t_{ee} (left) and $t_{\mu\mu}$ (right).

2.4 Sensitivity to $\Delta\alpha_{\rm had}$

The running of the electromagnetic coupling increases with the (space–like) momentum transfer, as illustrated in Fig. 2.9, which shows separately the leptonic and hadronic shifts, $\Delta\alpha_{\rm lep}(t)$ and $\Delta\alpha_{\rm had}(t)$. By elastic kinematics, larger $|t|$ maps to higher electron energy and thus to smaller θ_e; consequently, the sensitivity to $\Delta\alpha_{\rm had}$ is maximal at small angles (e.g. $\theta_e \lesssim 10$ mrad), while the large-angle, low-energy region ($\theta_e \gtrsim 30$ rad, $E_e \lesssim 1$ GeV) is essentially insensitive and can be used as a control sample. Considering the kinematics of MUonE one typically has $\Delta\alpha_{\rm lep} \sim 10^{-2}$ and $\Delta\alpha_{\rm had} \sim 10^{-3}$, with the hadronic term falling to $\sim 10^{-5}$ at large θ_e.

To quantify the sensitivity to the hadronic contribution one defines

$$R_i(\theta_i) \;=\; \frac{d\sigma_i(\Delta\alpha_{\rm had} \neq 0)/d\theta_i}{d\sigma_i(\Delta\alpha_{\rm had} = 0)/d\theta_i}, \tag{2.23}$$

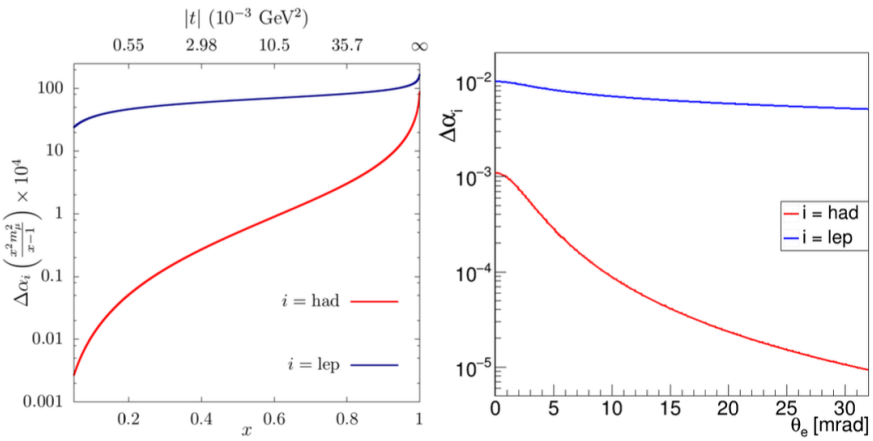

Figure 2.9: Running of α vs. x and t (left) and vs. θ_e (right). $\Delta\alpha_{\text{had}}$ in red, $\Delta\alpha_{\text{lep}}$ in blue [23].

i.e. the ratio of the differential cross section including vs. excluding the hadronic running.
At LO the effect factorizes as

$$\frac{d\sigma}{dt} = \frac{d\sigma_0}{dt}\left(\frac{\alpha(t)}{\alpha}\right)^2 = \frac{d\sigma_0}{dt}\frac{1}{\left|1-\Delta\alpha(t)\right|^2} \simeq \frac{d\sigma_0}{dt}\left(1+2\,\Delta\alpha(t)\right), \tag{2.24}$$

so R_i directly traces the running. At NLO, the sensitivity is reduced due to the presence of the radiative corrections, like the photon emission by the scattered electron. A tight acoplanarity selection allows to select events with two bodies in the final state and to reject the radiative processes.

Although the region where $\Delta\alpha_{had} \lesssim 10^{-5}$ carries essentially no direct sensitivity to the hadronic running, it plays a strategic role in the measurement. In practice, this phase space serves as a normalization region, enabling an evaluation of the running of α with minimal dependence on an absolute luminosity determination. A distinctive strength of MUonE is that the same elastic process provides both the signal (small-angle, high-$|t|$) and the normalization (large-angle, low-$|t|$) samples within a single apparatus and dataset. Forming ratios of event yields between these two regions cancels many detector and efficiency systematics, thereby stabilizing the extraction of the hadronic contribution.

These sensitivity and normalization considerations translate directly into detector requirements for sub-mrad angular resolution and minimal material, motivating the tracking system outlined below.

2.5 Tracking system

The MuonE experiment concept is based on the precise measurement of the muon and electron scattering angles with respect to the incident beam direction.
The setup is conceived as a succession of identical stations that turn the incoming muon beam into a precise angular reference. Since muons in the M2 beam are very energetic (160 GeV), they cross the apparatus with only a few MeV of energy loss per station, and with negligible degradation of direction. This behavior allows the same beam to be effectively reused along the entire detector chain, keeps the thickness of each individual beryllium or graphite layer small, and spreads the statistics of all $\mu - e$ elastic scattering events across the full array of detectors.

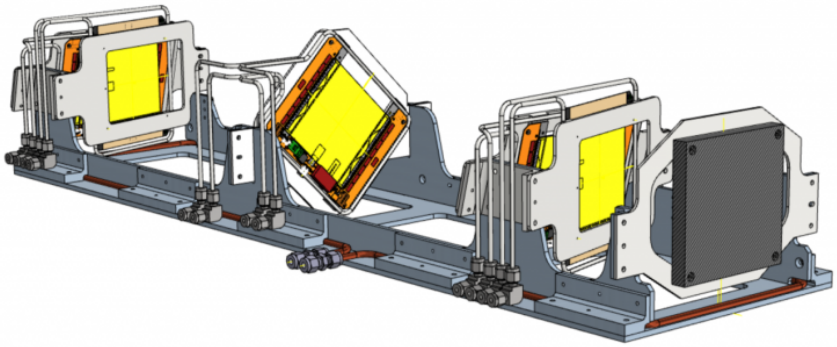

Figure 2.10: CAD drawing of a tracking "gondola" pertaining to an individual tracking station (see text). The muon beam propagates from right to left hitting the target (black). The tracks of the scattered particles are then recorded by the 2S modules (yellow).

Within this modular design, the basic unit of the tracking system is the single gondola, sketched in Fig. 2.10, which is mounted on a positioning system and enclosed in an environmental box to form a station. Each gondola behaves as an independent detector built around one low-Z target and six tracking modules. To select elastic events with high purity, the tracker must deliver an angular resolution of ~ 0.02 mrad [2]. With a gondola lever arm of approximately 1 m, the angular resolution requirement translates into a spatial single hit resolution of ~ 20 µm. With the above gondola lever arm, a detector active area of about 10×10 cm^2 is sufficient to contain all kinematically relevant events, since the geometrical acceptance is found to be ~ 50 mrad. In addition, the detector should combine high detection efficiency, high rate capability at the 50 MHz level expected on the M2 beamline, and a favorable signal-to-noise ratio.
In light of these considerations, the chosen tracking detectors are the "2S modules" designed for the high luminosity LHC upgrade of the CMS tracker [28].

An individual 2S module is composed of two single-sided, 320 µm thick, silicon micro-strip sensor planes. Each plane has a total of 1016 strips with a 90 µm pitch, read out by eight CMS Binary Chips (CBC) [29], for a total area of 10×10 cm^2. The two micro-strip sensor planes are separated by about 1.8 mm and have parallel strips measuring the same coordinate. The CBC front-end correlates clusters across the plane pair forming a "stub" when a match is found. The chip provides a binary measurement, presence or absence of a hit. Within a gondola, two modules read out the x coordinates, two the y coordinates, and the remaining two form a stereo pair at about 45° around the z axis, which resolves ambiguities and stabilizes pattern recognition during track formation.
While stereo modules are orthogonal to the z axis of the gondola, which is chosen to coincide with the beam direction, the x and y modules are tilted by about 233 mrad. This setting has been optimized after a detailed simulation study and increases benign charge sharing, raising the fraction of tracks which produce signals in two adjacent strip from a few percent to roughly 40–50% (threshold-dependent) and improving the single hit resolution from 26 µm, corresponding to the strip pitch, toward 10 µm [30].
The capability to separate the outgoing muon from the electron depends on the tracker angular resolution. When the intrinsic angular uncertainty grows, the kinematic region where the two leptons have similar angles becomes wider and misidentification increases.

Fig. 2.11 shows the distributions of the two scattering angles θ_{left} and θ_{right} for events simulated with ideal and realistic angular resolution, limited only by MCS effects from the target, without prior particle identification. The green points indicate events with incorrect or swapped particle identities, while the blue ones represent events with correct PID. In the region where they overlap, it is challenging to determine particle identities using only the tracker. This stresses that the tracker alone is insufficient for efficient PID and that information from the ECAL and the MF is essential for reliable particle identification.
To shrink the ambiguous angular region and reach the required precision, the tracker geometry must remain exceptionally stable. In practice, the longitudinal distances between tracking planes within each gondola have to be controlled at the level of 10 µm. Any uncertainty in the estimation of the relative module positions propagates into track parameters and, ultimately, into the two reconstructed scattering angles. For this reason, several precautions have been taken. The gondola structure is made of Invar, an alloy with a very low thermal expansion coefficient ($\sim 1.2 \times 10^{-6}$ K^{-1}), and a distilled water cooling circuit kept at $\sim$ 18 °C runs near the sensor edges, in

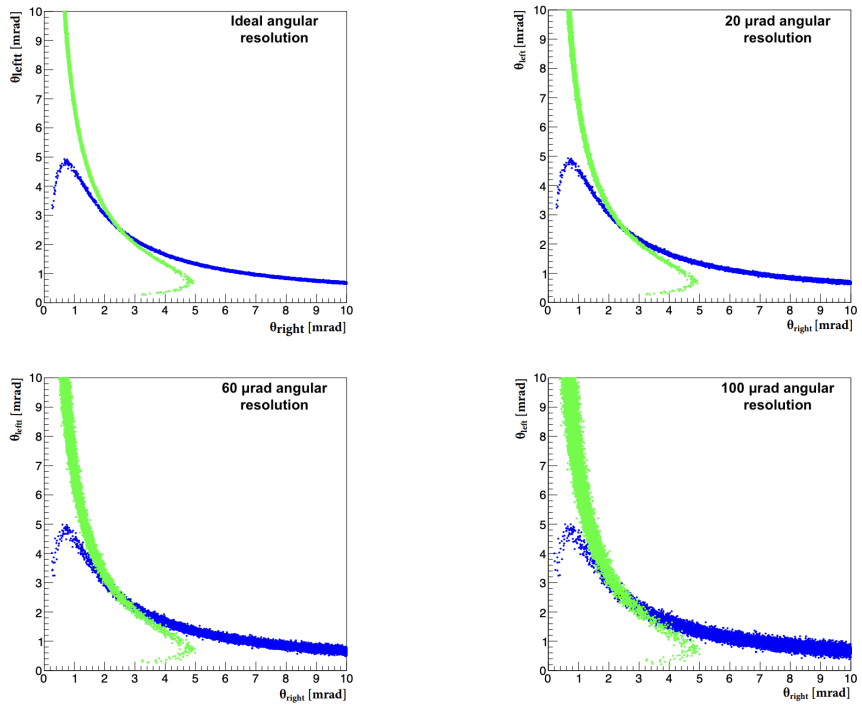

Figure 2.11: Distribution of the two measured scattering angles for events simulated with different angular resolution: (top-left) ideal angular resolution (only MS effect from the target, see text); (top-right) angular resolution of 20 µrad; (bottom-left) angular resolution of 60 µrad; (bottom-right) angular resolution of 100 µrad. The blue points correspond to correct particle identification, while the green points indicate incorrect identification [25].

order to dissipate the heat generated by the front-end electronics.

The gondola, together with its motorized movable supports, is then housed in a sealed light-tight box where the temperature is actively regulated to within about ±1 °C with dry filtered air to keep humidity low. Finally, as visible in Fig. 2.12, the stations are placed inside a large thermally isolated enclosure also flushed with constant temperature dry air.

The geometric stability can then be directly checked during data taking intervals. The Holographic Alignment Monitor (HAM) has been developed for this purpose. It based on a digital holographic interferometer, implemented in a lens-less off-axis configuration, which is able to monitor relative displacements and deformations in the mechanical structure with sub-micron accuracy [31].

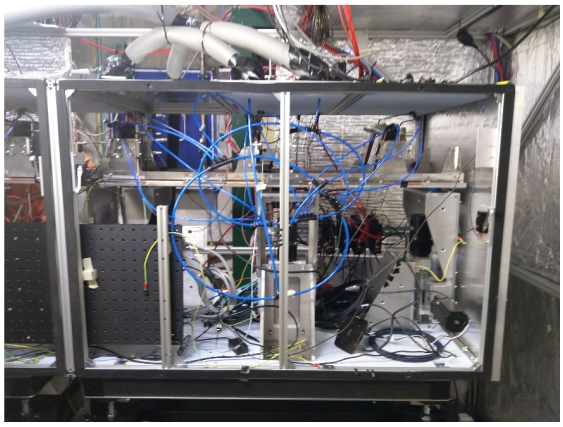

Figure 2.12: Photograph of a MUonE tracking station with side covers removed. The gondola is visible inside, suspended on a three-point motorized support system. Note the large environmental enclosure surrounding the station (see text).

2.5.1 Holographic Alignment Monitor

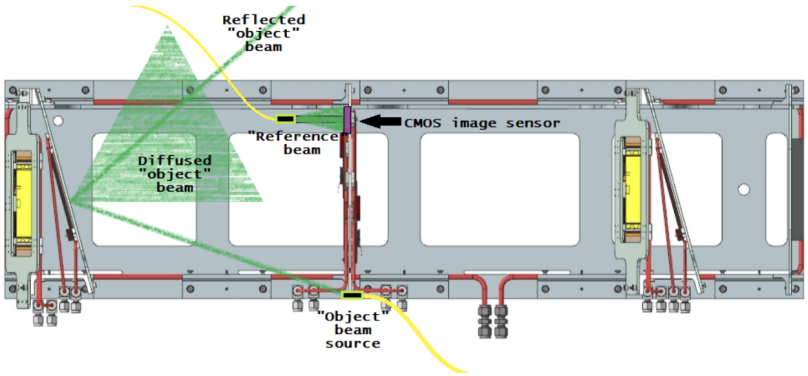

Figure 2.13: Schematic diagram of the Holographic Alignment Monitor mounted on a MUonE station.

HAM is a time-resolved interferometric technique based on off-axis lens-less digital holography [32]. It works by splitting the 532 nm light emitted by a fiber-coupled laser into two coherent beams. The "reference" beam is routed to illuminate directly a CMOS pixel sensor, while the "object" beam illuminates the active surface of the tracker; the diffusely reflected light propagates back to the same photosensor. The superposition of the two fields on the sensor forms an interference pattern that is recorded as a raw hologram. Each image acquired at time t_n (n$\geq$1) is digitally superimposed on the reference one taken at t_0 and then reconstructed via a Fast Fourier Transform (FFT) based algorithm. In this way, the possible displacement of a tracking plane with respect to the u-v frame is monitored by observing the interference fringes

that appear in the reconstructed holographic image. Each fringe corresponds to a displacement of half a wavelength. The HAM schematic on a CAD drawing of the MUonE tracking station is shown in Fig. 2.13.

2.6 Electromagnetic calorimeter

In the MUonE beamline an Electromagnetic CALorimeter (ECAL) is placed downstream of the last target–tracker station, see Fig. 2.3. It consists of a 5×5 array of $PbWO_4$ crystals, similar to those used for the electromagnetic calorimeter of the CMS experiment [33]. The scintillation light is read-out by Avalanche PhotoDiodes (APDs), while the front-end electronics is based on the multi-gain preamplifier (MGPA) chip [34]. Figure 2.14 shows the array of bare crystals of the ECAL mounted in their support lattice.

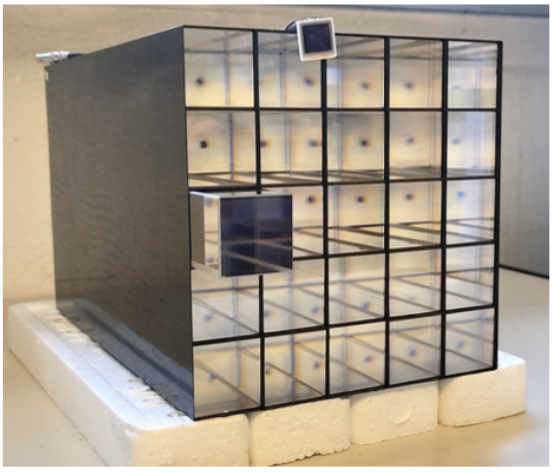

Figure 2.14: Photograph of the array of bare crystals at the heart the MUonE ECAL with a single crystal displaced out of position for illustration purposes. One of the APD sensors used to detect the scintillation light is shown at the top of the structure.

The inclusion of the ECAL in the MUonE apparatus contributes to the following [2][35]:

- an independent measurement of the electron energy;
- μ/e particle identification, especially in the kinematic region where $\theta_\mu \approx \theta_e$, achieved by analyzing the electromagnetic showers;
- direct identification of radiative or background events;
- systematic studies.

2.7 Muon filter

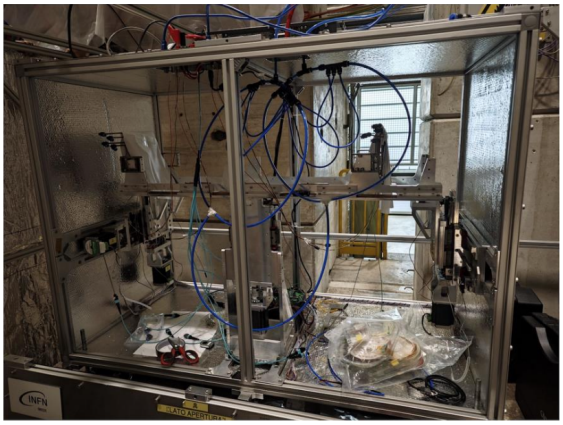

Figure 2.15: Photograph of the Muon Filter.

The Muon Filter (MF) is positioned downstream of the ECAL and consists in principle of two tracking planes separated by a given distance each giving the (x, y) coordinates of a particle hit. Its purpose is to provide efficient particle identification by tagging penetrating muons, and to supply precise track measurements after the ECAL that can be linked back to the upstream tracks. In elastic μ–e events, the tracks reconstructed in the MF are extrapolated back to the last tracker station to confirm the muon labelling hypothesis. This procedure increases the muon track identification efficiency, and it is especially useful in the angular region, typically below 5 mrad, where the trackers alone do not separate electrons and muons unambiguously.

For the 2025 run, the MF has been implemented in a "baseline" configuration consisting of two $x - y$ tracking planes spaced by about 60 cm, each plane formed by two 2S modules identical to those used upstream in the standard tracking stations. This initial choice of detectors for the MF is motivated by the advantage of a seamless integration with the global DAQ of the experiment. Since the hardware is identical to that of the tracking stations, only the greater downstream distance, and hence the different time delays, need to be accounted for when assembling the data stream.

In addition, the active area of the 2S modules, about 10×10 cm^2, still provides sufficient geometric acceptance when positioning the MF downstream of the three-station plus ECAL beamline arrangement used in the 2025 test run. With a characteristic angular spread $\lesssim 5$ mrad for elastically scattered muons, the expected transverse offset at ≈ 3 m from the initial target is only $\approx$ 15 mm, which remains well within the 50 mm half-width of the 2S module sensitive area.

For the final MUonE experiment apparatus, which will include up to 40 stations upstream of the electromagnetic calorimeter, the 2S planes in the MF will be replaced by scintillating fiber

tracking planes (SciFi MF). This proven technology offers a scalable active area and, in the final configuration, will cover about 51.2×51.2 cm^2, matching the larger geometric acceptance required at the end of the extended MUonE setup.

2.8 DAQ system

The MUonE data acquisition system is derived from the CMS Phase-2 tracker read-out [28] but adapted to the M2 beam, where muons arrive asynchronously compared to the 40 MHz clock, generating signals with random phases relative to it. Consequently, stub data from the 2S modules are streamed continuously without a hardware trigger at the front end; online selection is deferred to firmware in the back end. At module level, the CBC finds and formats stubs at 40 MHz, the CIC aggregates eight clock cycles prioritizing low-bend candidates (thereby favoring small-angle tracks), and packets are transmitted via lpGBT optical links [36] to the off-detector read-out. In MUonE the "bend" field, used as a pT tag in CMS, effectively serves as a direction/angle discriminator in the absence of magnetic field, helping early rejection of large-angle or noisy activity while preserving the compact stub representation.

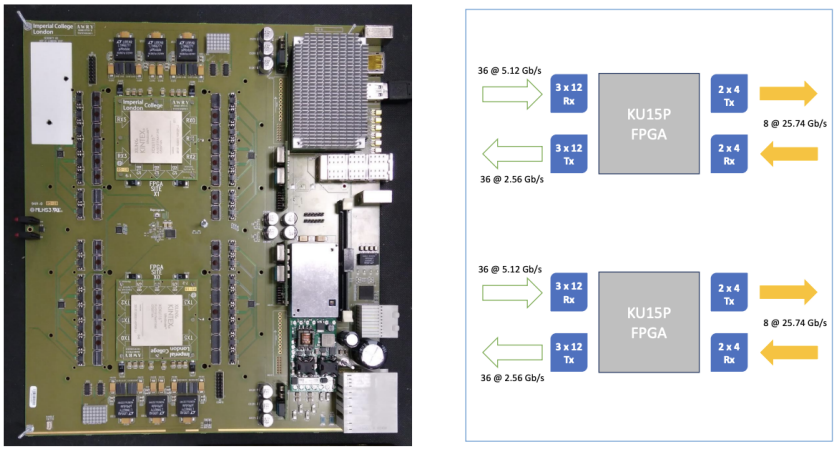

Figure 2.16: The CMS ATCA Serenity platform, with two FPGA daughtercards mounted on interposers. The integrated CPU Computer-on-Module is visible at top-right (left). Diagram illustrating the Serenity configuration for MUonE (right).

The Serenity development platform [37] (Fig. 2.16), developed for the CMS Phase 2 upgrade, is used to control and read-out data from the 2S modules.

The board is equipped with two Xilinx KU15P FPGAs [38] and multiple high-speed optical

links. Each KU15P provides 36 bidirectional detector I/O links and additional 25 Gb/s ports for networking and inter-board traffic. A single Serenity board will be able to control up to 72 2S modules, namely 12 stations. Consequently, 4 Serenity boards are adequate to read-out the full detector composed of 40 stations.

During the 2023 test run, about 350 TB of raw data were recorded over one week without any online filtering, and the synchronous read-out of two independent systems (tracker and ECAL) was demonstrated. The run also explored methods for online event selection, yielding guidance on how to reduce future demands on data storage and processing.

In a high-intensity beam with many tracking planes, the detectors produce raw data at a rate that cannot be written to disk in full. The probability for a muon to interact elastically in a single target is about one in three thousand, so only a small fraction of 40 MHz clock cycles carries information relevant to the physics program. Two online selection strategies are therefore adopted on the Serenity FPGAs: the first uses simple occupancy cuts, while the second performs a fast track reconstruction with optional vertexing to refine the accepted sample. At the highest uniform M2 intensity the instantaneous muon rate reaches about 50 MHz during a spill of five seconds. The average muon multiplicity per 25 ns cycle is then 1.25. Events with at least one muon crossing a tracking station occur at about 30 MHz, but most of these contain no elastic interaction in the target: by selecting only cycles compatible with a scatter, the quantity of data stored to disk can be reduced by orders of magnitude. A pre-scaled sample of through-going muons is nevertheless retained for alignment and detector monitoring. Events with a multiplicity of 1 contribute approximately 50 % of the elastic events with the cleanest signature [2]. The remaining 50 % contain an interacting muon with pile-up muons. Consequently, the online filter should identify elastic scattering of single muons as well as with those with pile-up. An elastic scatter downstream of the target yields one track from the scattered electron and one from the secondary muon. The downstream tracking planes therefore contain more hits than the upstream planes. The cleanest signature uses one hit in each upstream plane and two hits in each downstream plane. To increase robustness against noise and module inefficiencies, the requirement is relaxed to allow up to one missing hit in a downstream plane. The selection efficiency on signal events has been evaluated with simulated NNLO elastic scattering. Matching occupancy patterns already provides strong rejection. The Serenity resources also permit online tracking to enhance the decision. Real time reconstruction is split into a finding stage, which assembles hit candidates into track seeds, and a fitting stage, which estimates track parameters as straight lines in the MUonE geometry. The fitting stage was demonstrated on live data in 2023. Raw data are first recorded on CERN EOS. For redundancy a copy is transferred on a rolling basis to the INFN CNAF computing center, which also enables distributed analysis. The

decoding step then produces ROOT ntuples for analysis.

3 Simulation framework and event reconstruction

The MUonE simulation chain combines specialized Monte Carlo (MC) generators with the Geant4 toolkit [39]. For each run, the interaction vertex is placed in the configured target, while the incoming muon beam can be generated with realistic M2 momentum and transverse-profile distributions using prescriptions provided by CERN experts. The simulation outputs both truth-level particles and detailed hit/energy-deposit information in the detector materials, stored as ROOT TTrees for downstream digitization, reconstruction, and analysis.

3.1 Simulation

A detailed, geometrically accurate, simulation of the full MUonE setup is implemented in the FairMUonE software, built on the ROOT-based FairRoot framework [40] with Geant4 and other external packages via FairSoft. The same environment is used consistently across event generation, detector geometry description, detector response simulation (including sensor physics and readout behavior), digitization, reconstruction, alignment, and analysis. The geometry is easily configurable as the hardware evolves, for example in the number of tracking stations, the silicon module layouts, and the target type or thickness. This flexibility has been used to reproduce the 2025 test-run configuration.
Throughout the simulation, each generated particle is followed through all relevant materials (including air) in the detector geometry. Non-instrumented support structures outside the active region are typically omitted but can be restored if needed for systematic studies. In addition to signal and key backgrounds from the MESMER generator (Muon Electron Scattering with Multiple Electromagnetic Radiation), which is directly interfaced in FairMUonE, Geant4 can also be run in a *minimum-bias* mode to produce generic secondaries according to their cross sections.

For a 160 GeV muon traversing a light target such as beryllium, the background is dominated by electromagnetic processes beyond the elastic μe signal. The leading contribution is lepton–pair production in the nuclear Coulomb field, $\mu N \to \mu N \ell^+\ell^-$, with $\ell = e, \mu$, whose cross section scales approximately as Z^2 and therefore grows faster with atomic number than the elastic signal (which scales as Z). In practice, e^+e^- production is most frequent and can imitate elastic topologies if one lepton is soft or unreconstructed. Pair production on atomic electrons, $\mu e^- \to \mu e^- \ell^+\ell^-$, lacks the Z^2 enhancement and is smaller overall, but it remains relevant in a precision environment. Bremsstrahlung, $\mu N \to \mu N \gamma$ (and, less commonly, $\mu e^- \to \mu e^- \gamma$), provides another important channel: photons radiated by the muon may convert in nearby material,

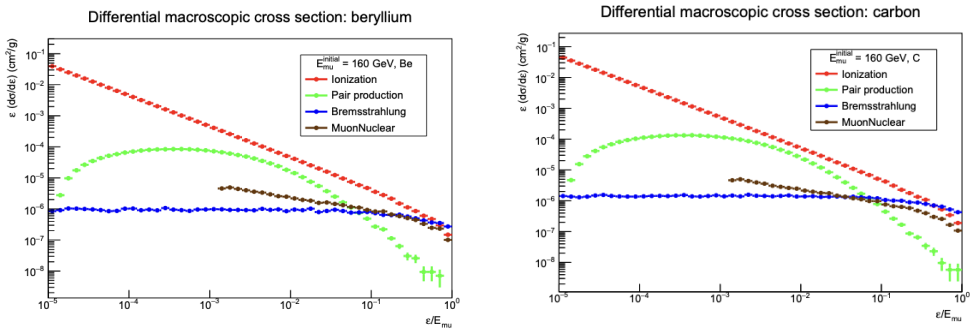

Figure 3.1: Differential macroscopic cross sections for muon interaction processes in beryllium (left) and carbon (right) as a function of the relative energy transfer ϵ/E_μ [39].

$\gamma N \to e^+e^-N$, creating trident-like signatures with vertices displaced downstream of the emission point. Inelastic interactions with nuclei, $\mu N \to \mu X$, are subleading in light targets at these energies, yet they can produce occasional hadronic activity that is useful for monitoring non-EM backgrounds. The differential behavior of these processes is illustrated by the macroscopic differential cross sections in beryllium at $E_\mu = 160$ GeV as a function of the relative energy transfer ϵ/E_μ (Fig. 3.1). Electromagnetic channels are soft-enhanced: bremsstrahlung follows a roughly $1/\epsilon$ trend, peaking at small ϵ/E_μ, while pair production likewise favors low transfers but extends to higher ϵ/E_μ as the e^+e^- pair becomes more energetic. Inelastic $\mu N \to \mu X$ contributes more visibly at comparatively larger ϵ/E_μ, though it remains subdominant in Be. This structure explains the prevalence of low-energy secondaries in data and motivates a careful treatment of soft radiation and conversions in the simulation.

3.2 Track reconstruction

The event reconstruction in FairMUonE takes as input the tracker stubs from data or from simulation. In the latter case, the stubs are produced during the digitization stage, which emulates the digital response of the 2S front-end electronics. Once the inputs are defined, the reconstruction proceeds with a pattern-recognition phase aimed at forming two-dimensional (2D) track candidates in the xz and yz projections. This set of 2D candidates is obtained by pairing hits from the x and y modules on the upstream and downstream planes of each tracking station. In certain kinematic configurations, the angular separation between the two outgoing tracks can be small in one of the projections, $\Delta\theta_{xz}$ or $\Delta\theta_{yz}$, so that the candidates may share one or more stubs. The algorithm accommodates this by allowing a configurable number of shared hits (typically between 0 and 2). The three-dimensional (3D) combination is then constructed by associating the stereo (u/v) measurements. The $\sim 45°$ rotation of the stereo modules about the

z axis facilitates a coherent matching of the xz and yz projections, thereby resolving ambiguities between nearly overlapping 2D candidates. For each pair of 2D tracks, the nearest stereo hit is searched within a window corresponding to 10 times the sensor resolution around the predicted impact point.
Given the two projected lines

$$x(z) = m_x\, z + q_x, \qquad y(z) = m_y\, z + q_y, \tag{3.1}$$

the expected coordinate measured by a stereo module rotated by an angle α at $z = z_{\mathrm{hit}}$ is

$$u_{\mathrm{pred}}(\alpha; z_{\mathrm{hit}}) = x(z_{\mathrm{hit}})\mathrm{cos}\alpha + y(z_{\mathrm{hit}})\mathrm{sin}\alpha. \tag{3.2}$$

The distance is then

$$d(\mathrm{hit}, \mathrm{track}) \equiv u_{\mathrm{hit}} - u_{\mathrm{pred}}(\alpha; z_{\mathrm{hit}}). \tag{3.3}$$

The selected stereo hit is added to the hit list associated with that 3D hypothesis. The 3D track parameters are then obtained by minimizing

$$\chi^2 = \sum_{\mathrm{hits}} \frac{[d(\mathrm{hit}, \mathrm{track})]^2}{\sigma^2_{\mathrm{hit}}}, \tag{3.4}$$

where σ_{hit} denotes the measurement uncertainty of the corresponding module.
In the elastic case under study, two outgoing tracks are reconstructed from a common target vertex. These tracks and their fit results provide the starting point for the vertex determination and for extracting the event kinematics.

3.3 Vertex reconstruction

For a given target, vertex candidates for elastic μ–e scattering are formed by combining one reconstructed downstream track with two reconstructed upstream tracks. All pairs of tracks are first examined to identify those whose extrapolations intersect within the target volume; for each such pair, a compatible incoming-muon track is then sought among the upstream segments. For

every complete triplet, a dedicated kinematic vertex fit is performed to determine the common point and to mitigate the impact of multiple scattering on the angular resolution.
MS is incorporated as an additional contribution to the uncertainty on the hit positions and directions. As an operational choice, the uncertainty is inflated on the track exhibiting the larger scattering angle in the outgoing pair (most often the electron at large angles). This is usually valid for $\gtrsim 5$ mrad, but may break down at smaller angles when the muon may occasionally carry the larger deflection. The multiple scattering contribution is estimated using the PDG/Highland expression [41]

$$\sigma_\theta = \theta_0 \cdot \Delta z = \frac{13.6 \text{ MeV}}{\beta\, p\, c} \sqrt{\frac{x}{X_0}} \left[1 + 0.038 \ln\Big(\frac{x}{X_0}\Big)\right] \cdot \Delta z, \tag{3.5}$$

where x/X_0 is the thickness in radiation lengths, Δz is the distance between the hit and the material encountered and the momentum p is estimated from the track angle using leading-order elastic kinematics.
The vertex position in the transverse plane is obtained by minimizing the sum of the squared, uncertainty-weighted distances of closest approach (DCA) of the three lines to a common point. The fit is formulated as a constrained least squares problem in which the free parameters are the slopes of the three 3D lines together with the vertex coordinates (x_v, y_v) (and, optionally, z_v). The objective function can be written as the sum of the trackwise contributions,

$$\chi^2_{\text{vertex}} = \sum_{i=1}^{3} \chi^2_{\text{track},i}, \tag{3.6}$$

where each $\chi^2_{\text{track},i}$ accounts for all hits used in the corresponding straight-line fit when constrained to pass through the common vertex. In low lever-arm configurations it is advantageous to fix z_v to the nominal target mid-plane to stabilize the solution; otherwise z_v is left free and determined by the fit.
After the common point is determined, the three tracks are refitted under the vertex constraint so that the fitted parameters and covariances are consistent with crossing (x_v, y_v, z_v). For events with more than two outgoing tracks, an analogous multi-track vertex fit is performed; in the absence of a reliable electron/muon identification at this stage, a symmetric multiple-scattering treatment is applied to all outgoing tracks. The resulting vertices are characterized by their fit quality, typically $\chi^2_{\text{vertex}}/ndf$, and by the compatibility of (x_v, y_v, z_v) with the known target geometry. These quantities are used to rank candidates within the same event and to discriminate elastic topologies from backgrounds such as pair production or secondary interactions.

3.4 Muon track identification

After the pair of outgoing tracks has been reconstructed and associated to a common vertex, the next step is to identify which track is the muon and which is the electron. At first, this assignment is made kinematically: within the pair, the track with the smaller scattering angle with respect to the incoming muon is labeled as the muon, while the other is labeled as the electron. This follows from elastic $\mu - e$ kinematics at MUonE energies, where the light electron typically recoils to larger angles and the muon is only mildly deflected. However, in the small-angle region the distinction becomes ambiguous. For this reason, the 2025 test run introduced the Muon Filter, absent in the 2023 configuration, with the explicit goal of providing an independent, downstream handle on particle identification. Operationally, the MF enables track labeling by linking trajectories upstream of the ECAL to hits recorded after the electromagnetic calorimeter. Since electrons initiate electromagnetic showers and are largely contained in the ECAL, while muons are minimum-ionizing and penetrate the calorimeter, hits in the MF are expected to arise predominantly from muons. The identification problem therefore reduces to a precise association between each reconstructed track and the MF hit pattern.
To perform this association in a way that is both efficient and quantitatively controlled, the Kalman filter is employed.
This method works in successive steps, as shown in Fig. 3.2. Starting from the tracks reconstructed in the stations upstream of the ECAL (Fig. 3.2a), the following sequence is applied:

- tracks in the last upstream station are propagated to the Muon Filter, accumulating multiple scattering from the traversed sensors and the calorimeter according to the material budget (Fig. 3.2b);
- if a MF hit lies within a given number of standard deviations N_σ, selectable by a specific variable in the code, the hit is added to the track;
- if a minium number of MF hits are associated to the track, then it is kept as a muon candidate;
- if two tracks share more than a maximum number of MF hits, the one with the worse MF-association χ^2 is discarded;
- surviving tracks are labeled as muons (Fig.3.2c);
- the identified state is then propagated upstream to the preceding station (Fig. 3.2d);
- if the propagated state matches a track in the upstream station within a given number of standard deviations, that track inherits the same label (Fig. 3.2e). Otherwise the state is

left untagged and the procedure continues;

- the propagation and match step is repeated station by station until the first station is reached;
- if the propagated state is compatible with two upstream tracks, a tie is resolved by comparing the association χ^2 values; if $\chi^2_{\text{worst}}/\chi^2_{\text{best}} >$ a given value, the best match is accepted, otherwise the case is flagged as ambiguous and no label is assigned.

A mathematical treatment of the Kalman prediction, update, and gating in this context is provided in Appendix A.

3.5 Kalman filter performance

The performance of the Kalman based muon identification has been evaluated on fully simulated samples, in which Monte Carlo truth is available. The goal is to quantify the trade-off between selection tightness and performance when associating reconstructed tracks to the Muon Filter and propagating the muon label to the downstream stations. The study scans the main reconstruction parameters that govern the MF association:

- the gating width, expressed in units of the predicted-position uncertainty;
- the minimum number of required MF hits;
- the number of shared hits between two tracks.

For each event, counts are accumulated as follows:

- **true positives (TP)**: real muons correctly identified as muons;
- **false positives (FP)**: non-muons incorrectly identified as muons;
- **false negatives (FN)**: true muons not identified as muons;
- **true negatives (TN)**: non-muons correctly rejected.

Performance is summarized in terms of *purity*, which measures the fraction of identified muons that are actually true muons, and *efficiency*, which measures the fraction of real muons that are correctly identified, defined as

$$purity = \frac{TP}{TP + FP} \qquad efficiency = \frac{TP}{TP + FN}. \tag{3.7}$$

The results of the simulation study are summarized in Table 1, which shows that the muon tag is

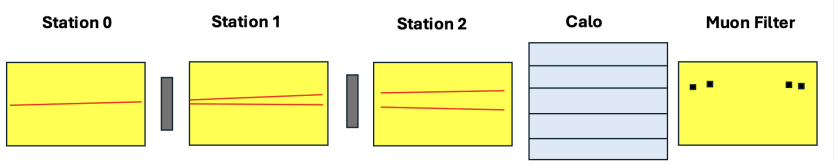

(a) Downstream tracks reconstructed and MF hits visible upstream.

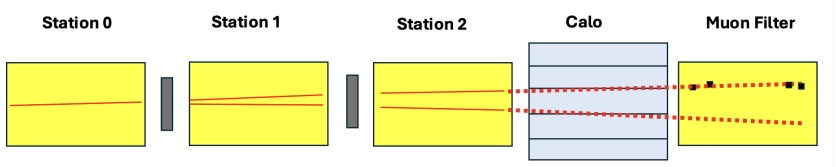

(b) Kalman propagation to the MF through ECAL and sensors; search for compatible MF hits.

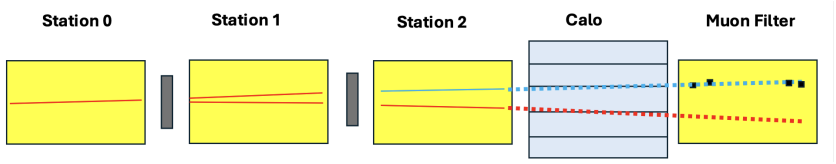

(c) MF association and muon tagging (blue track).

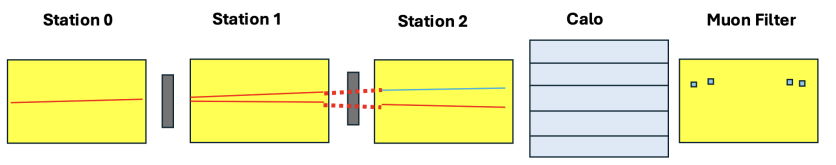

(d) Downstream propagation of the tagged state to the previous station.

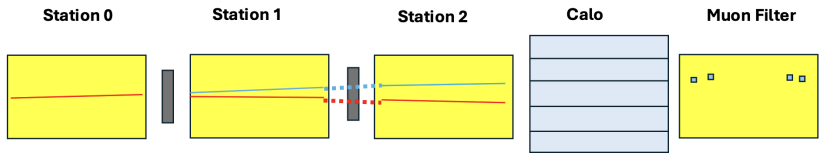

(e) Track-to-track matching in the downstream station.

Figure 3.2: Steps of the Kalman filter reconstruction in the case of only three stations, see also text [42].

intrinsically very clean in simulation: purity remains $\simeq 100\%$ across all working points with three required MF hits and either zero or one shared hit. Tightening the gate lowers the acceptance, with the efficiency passing from $\simeq 99.3\%$ for $N_\sigma = 5$ to $\simeq 40\%$ for $N_\sigma = 1$.

Cases with more than two shared hits are excluded from the scan because the association between competing tracks and MF hits becomes too ambiguous.

These considerations motivate the baseline choice $N_\sigma = 5$, a minimum of 3 MF hits, and no

N_σ	Min MF hits	Shared hits	Purity	Efficiency
5	3	0	1.000	0.993
4	3	0	1.000	0.990
3	3	0	1.000	0.981
2	3	0	1.000	0.887
1	3	0	1.000	0.400
5	2	0	0.997	0.997
4	2	0	0.998	0.997
3	2	0	0.998	0.995
5	3	1	1.000	0.993
4	3	1	1.000	0.990
3	3	1	1.000	0.982

Table 1: Purity and efficiency for different reconstruction parameters.

shared hits for the analysis.

4 2025 Test run

A test run with a reduced setup consisting of three tracking stations, followed by the ECAL and the MF, was conducted in July-August 2025 at the M2 beamline at CERN, which provided 160 GeV muons. The objectives of the run were to test integration and synchronization between different detectors in the chain and to check the efficiency with which elastic $\mu - e$ events are identified and recorded.
During the 2025 test run, data taking was handled by a DAQ chain derived from the CMS Phase-2 tracker readout and adapted to the asynchronous M2 beam. In this configuration, the 2S front-end continuously forms and streams stubs without a hardware trigger; event selection is deferred to the back-end firmware/software, which provides a menu of trigger selections.
Online performance was monitored in the Grafana environment [43]. Fig. 4.1a shows the Grafana overview dashboard with the rates of all trigger selections. Fig. 4.1b shows the focused view that tracks the selection used in this analysis, "1 single passing muon", characterized by hit patterns consistent with one incoming muon and two reconstructed outgoing tracks, potentially indicating an interaction within the target. The dataset considered here is restricted to interactions in the station 2 target.

Building on this online selection, the offline reconstruction proceeds in two steps. First, a *fiducial selection* is applied to enforce a clean event configuration consistent with the "1 single passing muon" trigger. Events are required to contain exactly one reconstructed track in station 0 and station 1, and two reconstructed tracks in station 2. For uniform acceptance and quality, each track must have exactly six hits, i.e. one hit per module in its station. This pre-selection suppresses edge regions and high-multiplicity backgrounds while keeping the elastic pattern expected for interactions in the station 2 target.
Fig. 4.2 shows the 2D kinematic distribution of the scattering angles observed in events of a given run before and after a basic elastic selection. Here, no vertex reconstruction selections ("vertexing" in the following) has yet been applied to the data points. The *elastic cuts* aim to select a sample of elastic events as clean as possible. Several requirements are applied:

- to suppress spurious reconstructions and non-Gaussian tails, it is required that both outgoing tracks satisfy $\chi^2/ndf < 20$;
- an acoplanarity cut is applied. This parameter quantifies the deviation from the back-to-back configuration in the transverse plane with respect to the incoming-muon direction. Denoting by $\hat{\imath}$ the unit vector of the incoming track and by $\hat{m}$ and $\hat{e}$ the unit vectors of the

(a) Rates for the full trigger menu to monitor stability.

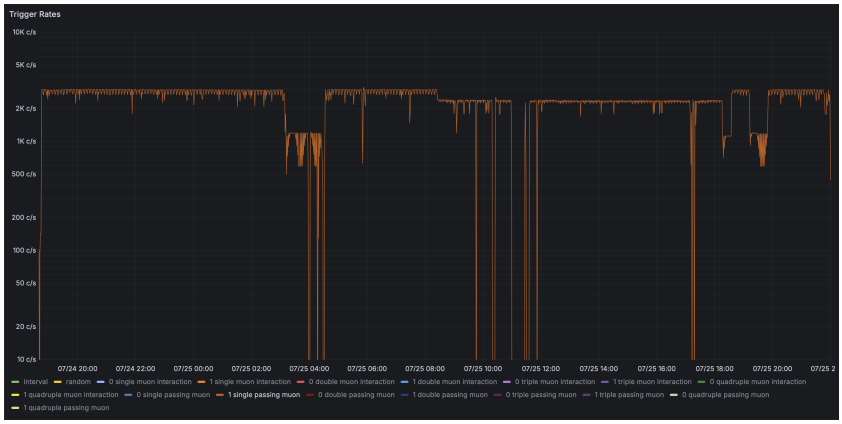

(b) Focused view of the "1 single passing muon" selection used in the analysis.

Figure 4.1: Grafana overview dashboard during the 2025 test run.

two outgoing tracks (muon and electron), the acoplanarity parameter is defined as

$$A_\phi \;=\; \pm\left[\pi \;-\; \cos^{-1}\left(\frac{(\hat{\imath}\times\hat{m})\cdot(\hat{\imath}\times\hat{e})}{|\hat{\imath}\times\hat{m}||\hat{\imath}\times\hat{e}|}\right)\right],$$

where the sign is fixed by

$$T \;=\; \hat{\imath}\cdot(\hat{m}\times\hat{e}) \qquad \Rightarrow \qquad \mathrm{sign}(A_\phi) = \mathrm{sign}(T).$$

For ideal elastic events one expects $A_\phi \simeq 0$ up to detector resolution; the operational

requirement is

$$|A_\phi| < 0.4.$$

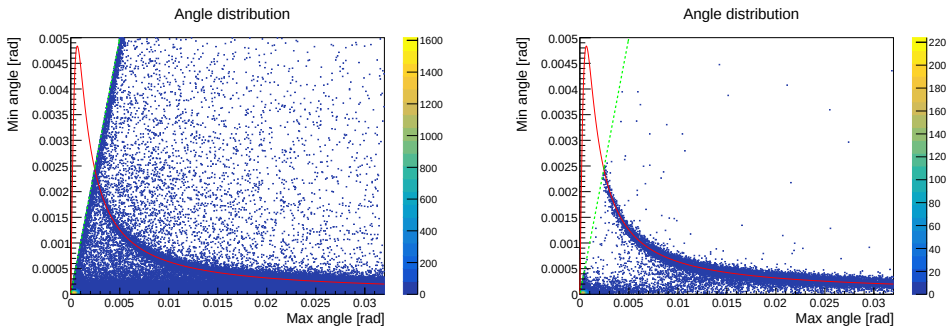

Figure 4.2: Pre-vertexing 2D distributions of the outgoing scattering angles with respect to the incoming muon direction before (left) and after (right) elastic selection, see text.

Before the elastic selection, the left panel in Fig. 4.2 shows a substantial background population, most evident at low θ_{min} and away from the expected elastic curve. After applying the elastic requirements the right panel exhibits a clear reduction of these contributions while the elastic band remains prominent. The red curve indicates the theoretical elastic relation for incoming muons of $E_\mu = 160$ GeV and serves as a reference for the signal region. The dotted green bisector line ($\theta_{max} = \theta_{min}$) marks the boundary below which the assignment of the two outgoing tracks is ambiguous in the absence of particle identification. By construction, no events appear below the bisector in either panel.

To resolve this ambiguity, the Muon Filter has been introduced in the 2025 test run. Outgoing tracks are propagated with a Kalman filter to the MF planes and matched to the observed hits; the track whose propagated state is most compatible with the MF hits is tagged as the muon, while the other is identified as the electron (i.e the non-muon). This procedure removes the constraint of the labeling $\theta_{max} - \theta_{min}$, thereby allowing events to appear on either side of the bisector.

Fig. 4.3 shows the pre-vertexing distribution before the elastic selection when all cases are present: $\mu - e$, $\mu - \mu$, and $e^+ - e^-$ tracks. A significant population is visible both along and around the bisector, reflecting cases where the two outgoing angles are similar and the assignment is intrinsically ambiguous without PID.

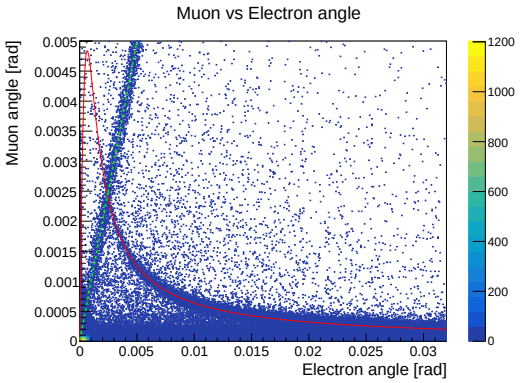

Figure 4.3: Pre-vertexing 2D distribution before elastic selection with PID. All cases are included, see text.

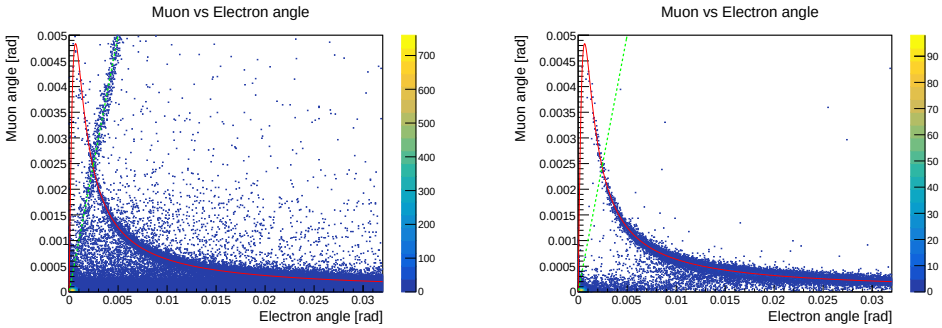

Figure 4.4: Pre-vertexing 2D distribution of muon vs electron scattering angles before (left) and after (right) elastic selection. Only $\mu - e$ cases are included, see text.

Restricting to $\mu - e$ pairs identified with the MF (Fig. 4.4) shows a concentration in the $\theta_\mu < \theta_e$ half-plane, consistent with elastic kinematics, while some population remains along the bisector due to small-angle symmetry and finite resolution.

After applying the elastic selection the $\mu - e$ sample tightens around the elastic curve and the bisector population is strongly suppressed.

A residual band of background remains visible in the μ–e category even after the elastic selection, particularly for $\theta_\mu \lesssim 3$ mrad. This structure is attributable to non-elastic interactions (e.g. radiative tails, conversions, secondary interactions) and to occasional small-angle mis-associations. Imposing a common-vertex constraint removes this band: requiring a well-fitted vertex built from the incoming direction and the two outgoing tracks, with z_{vtx} inside the station 2 target, suppresses non-target interactions. As a result, the distribution tightens around the expected elastic curve and the population along (and near) the bisector is strongly reduced.

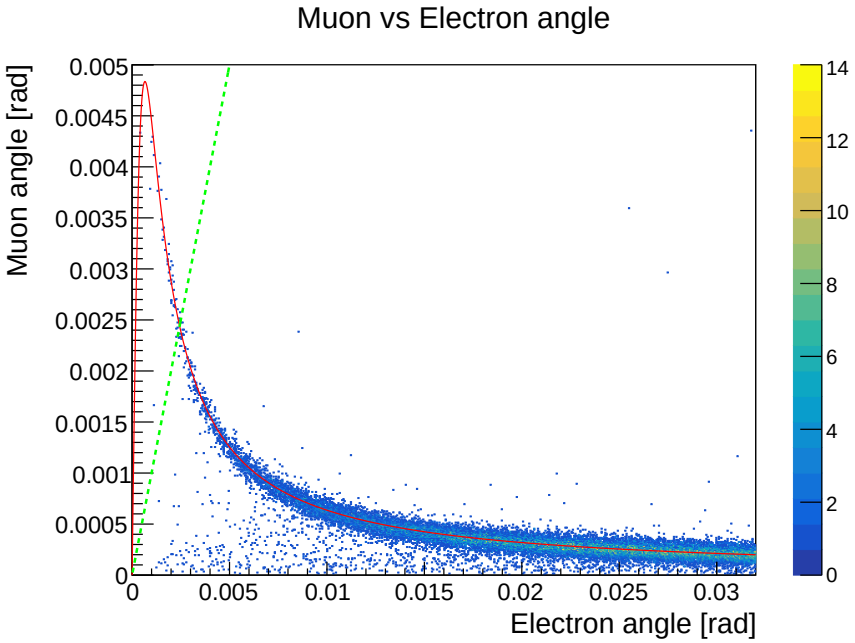

Figure 4.5: Post-vertexing 2D distribution of muon vs electron scattering angles after the final elastic selection. Only $\mu - e$ cases are included, see text.

Note in Fig.4.5 the clear appearance of data points correctly identified as elastic events even at low electron scattering angles below the bisector line.

For completeness, specific plot for the other cases ($\mu - \mu$ and $e^+ - e^-$ tracks) and from the simulations are shown in Appendix B.

5 Conclusions

The anomalous magnetic moment of the muon provides one of the most stringent tests of the Standard Model. Following the extremely precise measurement of the muon gyromagnetic anomaly recently obtained at Fermilab, and the remaining tensions in the theoretical landscape, a detailed knowledge of the hadronic contribution to the muon anomalous magnetic moment has acquired great importance.

The goal of the MUonE experiment is to obtain a precision measurement of the hadronic contribution by exploiting a space-like determination of this quantity, in a manner complementary to the current time-like approaches. This is achieved by measuring the electromagnetic coupling in the space-like region at low momentum transfer through the reconstruction of the $\mu - e$ elastic scattering.

The measurement is performed by scattering high energy muons on a low-Z target, exploiting the 160 GeV muon beam available at the M2 line at CERN, and obtaining with sub-percent precision the differential cross section of the $\mu - e$ elastic scattering process. The apparatus consists in a scalable string of individual tracking detectors, or "stations", each equipped with a thin target, followed by an electromagnetic calorimeter and a final downstream tracker without target, dubbed Muon Filter (MF). This last detector allows muon track identification in the small scattering angle region, where kinematical constraints alone cannot resolve electron and muon tracks.

Within this framework, the present work addresses muon track reconstruction and particle identification along the MUonE detector chain, with a special emphasis on the results obtained from the MF. A reconstruction strategy was adopted in which, starting from the MF, downstream particle identification information is consistently propagated upstream, enabling an unambiguous assignment of the muon candidate and a cleaner selection of elastic topologies. As noted above, this is most relevant in the small-angle region, where kinematic ambiguity limits the discriminating power of kinematics alone. The analysis of the data collected at CERN during the 2025 test run, combined with simulation results, shows that the Muon Filter is essential for reliable particle identification precisely in the ambiguity region at small scattering angles.

The final MUonE apparatus configuration will include up to 40 tracking stations before the electromagnetic calorimeter and the final MF. In this layout, the "2S" Si tracking modules used in the 2025 test run to equip the Muon Filter will no longer provide full angular acceptance. For this reason, a new "SciFi Muon Filter" is being developed, with tracking planes based on scintillating fibers. The transition to the SciFi system will require a re-optimization of the reconstruction and association method, so that the particle identification performance demonstrated in the test

run can be confirmed, and possibly improved, over the larger acceptance of the final apparatus.

Appendices

A Kalman filter

This appendix summarizes the linear Kalman filter used in MUonE for straight–line tracking with multiple scattering. The state is defined at a longitudinal coordinate z and collects transverse positions and slopes

$$X(z_1) = \begin{pmatrix} x \\ y \\ x_{slope,i} \\ y_{slope,i} \end{pmatrix}, \tag{A.1}$$

where the slopes are

$$x_{slope,i} = \frac{dx_i}{dz} \qquad y_{slope,i} = \frac{dy_i}{dz}. \tag{A.2}$$

Propagation from plane z_1 to z_2 uses the linear transport matrix A:

$$X'(z_2) = A_{1\to 2} X'(z_1), \tag{A.3}$$

with

$$A_{1\to 2} = \begin{pmatrix} 1 & 0 & \Delta z & 0 \\ 0 & 1 & 0 & \Delta z \\ 0 & 0 & 1 & 0 \\ 0 & 0 & 0 & 1 \end{pmatrix} \tag{A.4}$$

and Δz the separation between the two planes. The covariance is transported consistently, adding process noise

$$P_{pred} = APA^T + Q, \tag{A.5}$$

where **Q** models the uncertainty induced by multiple scattering:

$$Q = \begin{pmatrix} \theta_0^2 \Delta z^2 & 0 & \theta_0^2 \Delta z 0 & \\ 0 & \theta_0^2 \Delta z^2 & 0 & \theta_0^2 \Delta z \\ \theta_0^2 \Delta z & 0 & \theta_0^2 & 0 \\ 0 & \theta_0^2 \Delta z & 0 & \theta_0^2 \end{pmatrix}, \tag{A.6}$$

with θ_0 given by the PDG/Highland expression:

$$\theta_0 = \frac{13.6 \text{ MeV}}{\beta\, p\, c} \sqrt{\frac{x}{X_0}} \left[1 + 0.038 \ln\left(\frac{x}{X_0}\right)\right]. \tag{A.7}$$

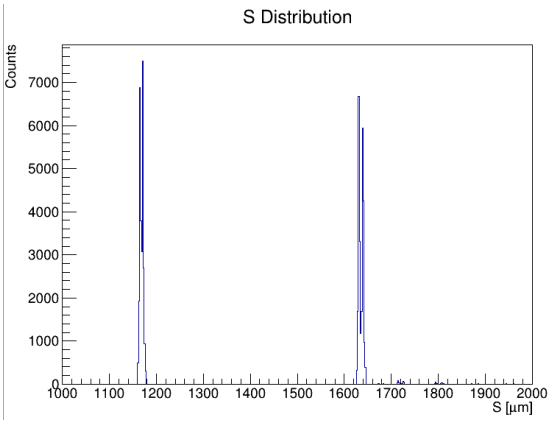

Figure A.1: Distribution of the innovation variance S for MF hits used in the Kalman association.

The measurement update balances the prediction with the observed hit through the Kalman gain K

$$K = P_{pred} H^T (H P_{pred} H^T + R_i)^{-1}, \tag{A.8}$$

where the measurement matrix for a 1D stereo hit at angle α is

$$H = \begin{pmatrix} \cos\alpha & \sin\alpha & 0 & 0 \end{pmatrix} \tag{A.9}$$

and $R_i = \sigma_i^2 = (26)^2$ µm is the hit variance (a typical value for the sensor resolution).

The state and its covariance are then corrected using the innovation

$$X'_{new} = X' + K(X_{measured} - HX') \qquad P_{new} = (I - KH)P_{pred}. \tag{A.10}$$

The per–hit contribution to the fit quality is evaluated from the χ^2:

$$\chi^2_{hit} = \frac{r^2}{S} = \frac{HX - X_{measured}}{HPH^T + R_i}. \tag{A.11}$$

In Fig. A.1 the distribution of S for Muon Filter associations is shown as a diagnostic of the combined process–noise and measurement model.

B Scattering angles distributions

This appendix documents control selections used to characterize backgrounds configurations under the same reconstruction and selection settings employed in Section 4.

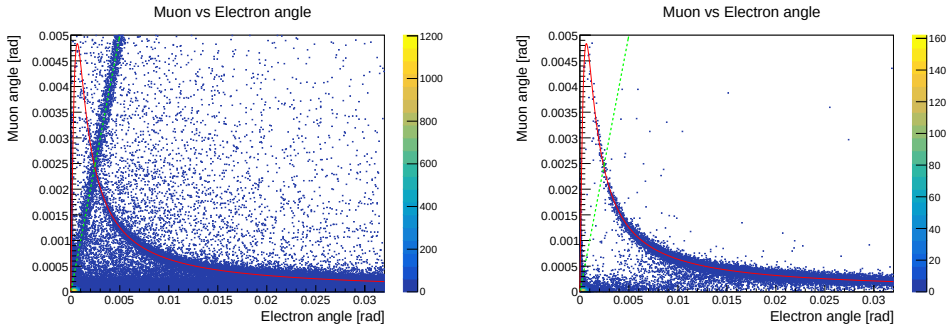

Figure B.1: Pre-vertexing 2D distribution before (left) and after (right) elastic selection with PID.

Fig. B.1 shows the pre-vertexing angle distributions when all PID categories are kept. Before elastic cuts a large occupancy is visible around the bisector and at low angles; after the elastic selection the population reduces but keeps contributions not compatible with the elastic curve, as expected when combining categories.

Fig. B.2 reports the e^+e^- control selection. Compared to the signal-like $\mu - e$ sample in Fig. 4.4 these events populate regions less correlated with the elastic curve.

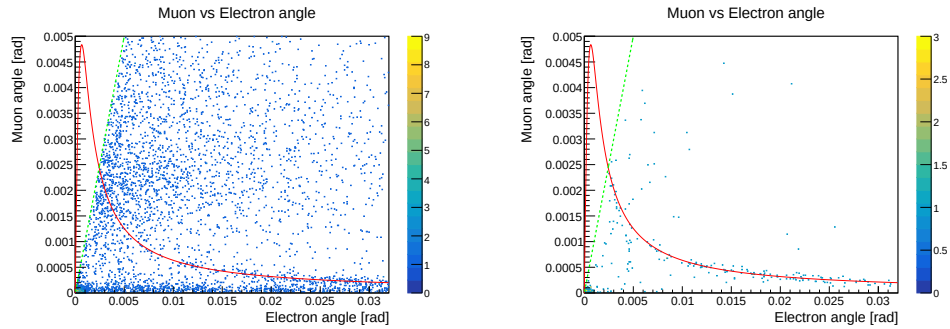

Figure B.2: Pre-vertexing 2D distribution of e^+e^- scattering angles before (left) and after (right) elastic selection.

Fig. B.3 reports the $\mu\mu$ control selection. Events cluster at very small angles and predominantly along the bisector, indicating nearly equal angular deflections for the two tracks. After the elastic

cuts this bisector population is strongly reduced.

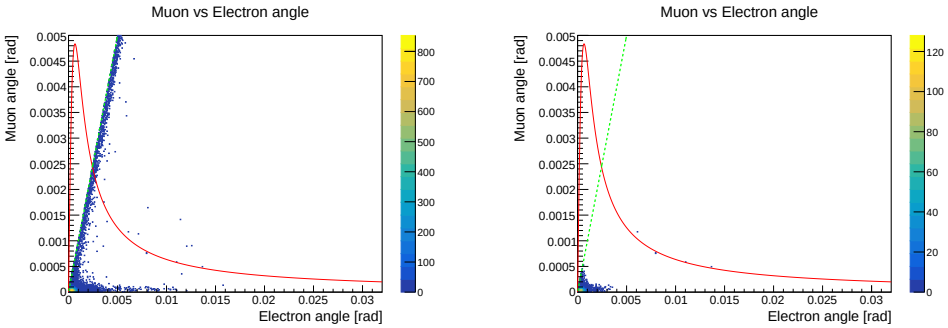

Figure B.3: Pre-vertexing 2D distribution of $\mu\mu$ scattering angles before (left) and after (right) elastic selection.

For completeness, Fig. B.4 summarizes the post-vertexing distributions when the vertex is required inside the station 2 target. In the $\mu\mu$ subset (not reported) only 3 events remain, indicating a very strong rejection of this class once the vertex constraint is enforced.

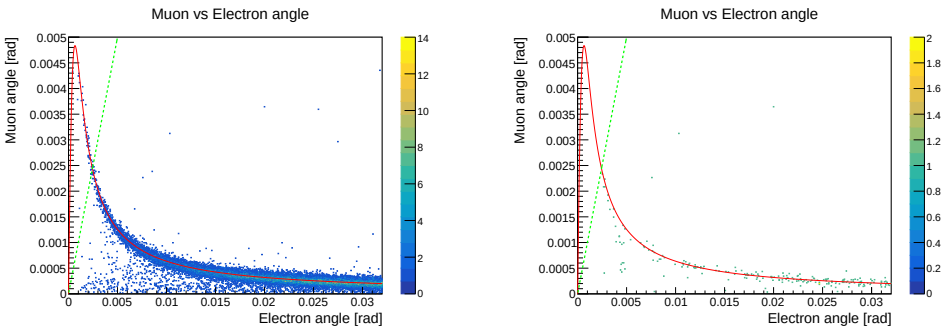

Figure B.4: Post-vertexing 2D distribution (left) and e^+e^- (right) scattering angles after elastic selection.

B.1 Simulation results

This subsection presents the same 2D angle distributions as in data, but derived from simulated events reconstructed with the identical workflow.

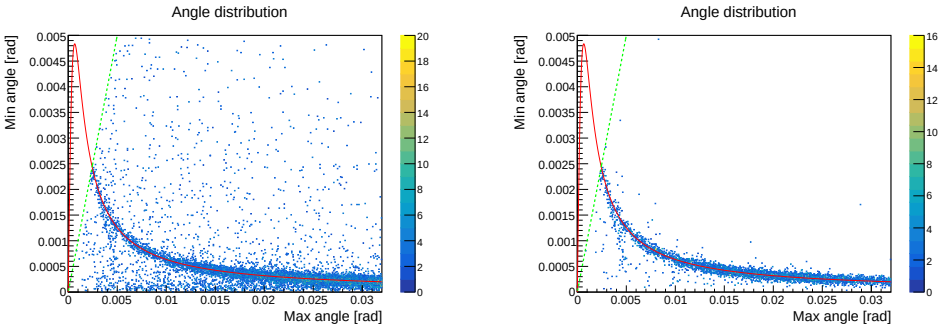

Figure B.5: Pre-vertexing 2D distributions of the outgoing scattering angles with respect to the incoming muon direction before (left) and after (right) elastic selection for simulated events.

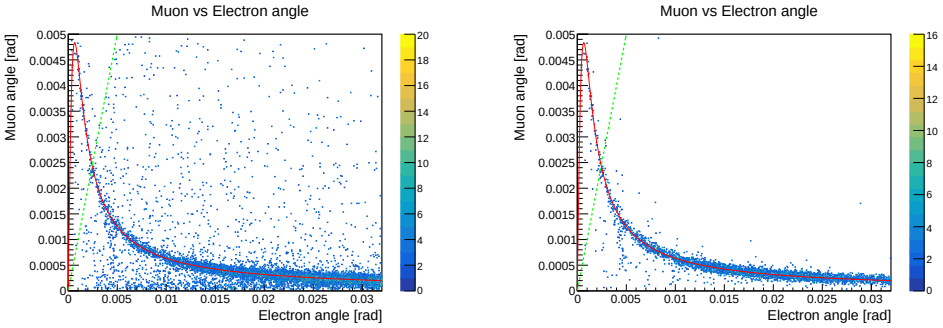

Figure B.6: Pre-vertexing 2D distribution before (left) and after (right) elastic selection with PID for simulated events.

The simulated samples reproduce the expected asymmetric topology of elastic μ–e scattering: already at pre-vertexing level the population lies away from the bisector ($\theta_\mu \simeq \theta_e$), with $\theta_e \gg \theta_\mu$. After applying the elastic selection, events concentrate along the elastic curve without developing a ridge on the bisector, consistently with the underlying kinematics.

Breaking down by PID category clarifies the pattern. The μe^- events concentrate around the elastic curve. The e^+e^- control sample shows weak correlation with the μe elastic locus and remains largely off-curve both before and after selection. The $\mu\mu$ control sample, which can generate nearly symmetric angles at very small deflections, is strongly suppressed once the elastic and vertex constraints are imposed, leading to a clean depletion along the bisector in the

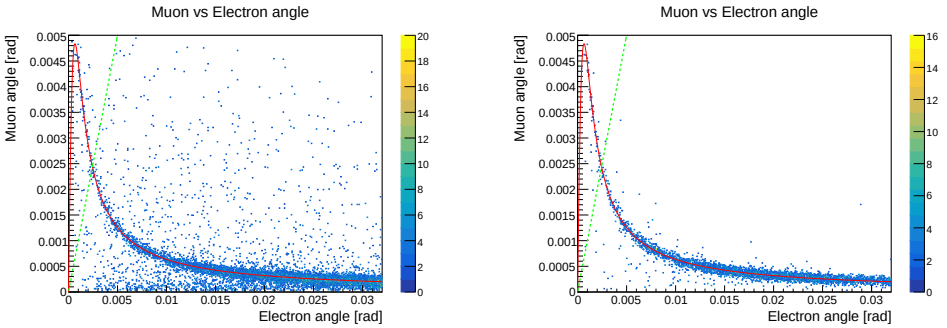

Figure B.7: Pre-vertexing 2D distribution of $\mu - e^-$ scattering angles before (left) and after (right) elastic selection.

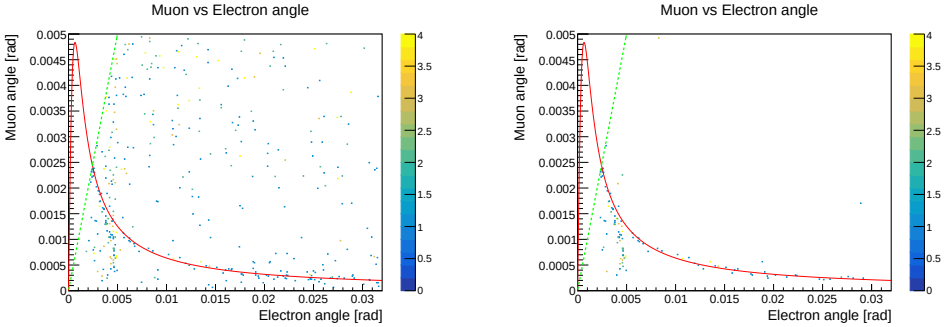

Figure B.8: Pre-vertexing 2D distribution of e^+e^- scattering angles before (left) and after (right) elastic selection.

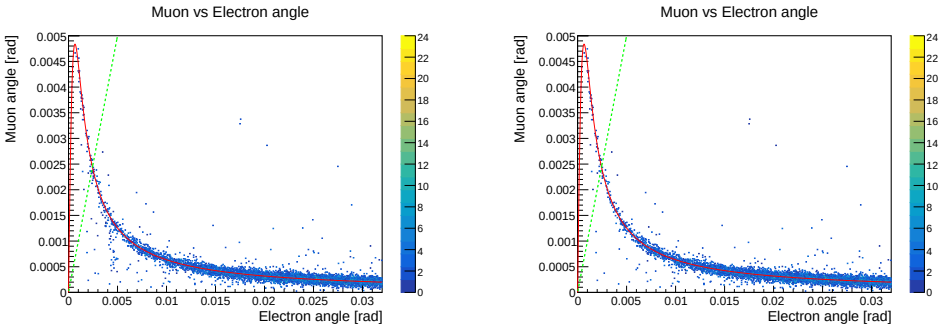

Figure B.9: Post-vertexing 2D distribution of all (left) and $\mu - e^-$ (right) scattering angles after elastic selection.

post-vertexing maps. Overall, the absence of a bisector component in simulation indicates that any bisector population observed in data originates from non-elastic backgrounds and/or reconstruction/combinatorial effects rather than from the elastic μe signal itself.

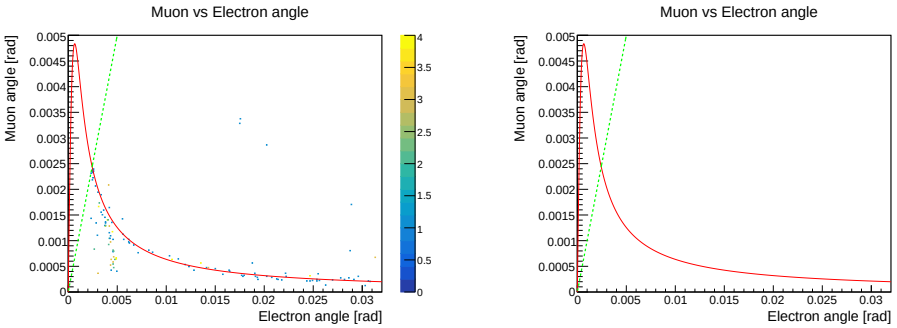

Figure B.10: Post-vertexing 2D distribution of e^+e^- (left) and $\mu\mu$ (right) scattering angles after elastic selection.

Ringraziamenti

Ci tengo innanzitutto a ringraziare il prof. Cantatore ed Aldo per il loro supporto e disponibilità lungo tutto il percorso.

Un ringraziamento speciale va ai miei genitori, che mi sono sempre stati vicini, soprattutto nei momenti in cui probabilmente nemmeno io ci credevo fino in fondo. Se oggi arrivo qui, è anche (molto) merito vostro.

Un mega grazie va a Frenga. Donna, ti conosco da troppo tempo ed entrambe sappiamo che delle due sei tu quella che esprime i sentimenti (probabilmente un po' troppo). So che non te lo dico mai abbastanza, ma grazie di esserci nella mia vita. Grazie a te ho capito che non tutti sono fatti per le materie scientifiche e che, per colpa delle ripetizioni di matematica e fisica che ti ho fatto alle superiori, ho probabilmente esaurito la mia scorta di pazienza per l'insegnamento. La carriera da prof era già destinata male.

Un super super grazie va ai miei Aspiranti ~~Fisici~~ Puttanieri: Cat, Annina, Leo, Fra, Pino, Gio, Stellina e Sevario. Vi ho conosciuto (chi prima e chi dopo) all'inizio di questo percorso pazzo. Sono convinta che senza di voi non mi sarei laureata e, anzi, avrei mollato quella che, ad oggi, spero sarà la mia carriera. Ho ancora gli incubi della prima sessione invernale tra H3 e Move, con lo studio dalle otto del mattino fino a mezzanotte: ora siamo diventati vecchi e (per fortuna) abbiamo capito che il fisico non regge. Seriamente: grazie per tutti i momenti e le serate passate insieme; anche se per metà del tempo ero mezza addormentata, le ho apprezzate davvero.
Tra di voi, un grazie speciale alle mie amichette Fra, Stella e Anna: mi siete sempre state accanto. Grazie.

Questo è decisamente un flusso di coscienza, quindi devo rettificare: ritmi simili sono (ahimè) tornati in tempi recenti. Di questo devo "ringraziare" il mio bellissimo gruppo di laboratorio, il Gruppo B(astardo). Fra Pizz, FraF, Fosco e Alby: siete la scoperta della magistrale. Con voi ho collezionato le gaffe fisiche più eclatanti (ricordiamo β), e non sono poche. Grazie per le pause in Eni e per la mia dipendenza dai toast, che sto cercando di superare (male). Un grazie speciale a Fosco, che ha tenuto particolarmente a farci uscire dal laboratorio alle 20 ogni giorno. I weekend a Foscolandia hanno aiutato a redimerti per questa tua brutta tendenza. Siamo partiti per studiare, abbiamo continuato per divertirci, la grappa alle alghe ha fatto la sua parte (grazie FraF per la scelta), e quando stava per subentrare la disperazione ci ha salvati la piscina.

Grazie a Gabriel e Tiziano che, insieme a Pino, mi hanno regalato una delle esperienze più assurde e belle: girare un corto giallo-western sulla scoperta del bosone di Higgs. Non so se mi

ricapiterà mai. A quando la materia oscura?

Un mega grazie va a tutti gli amichetti della T26 (non vi elenco, così non rischio figuracce dimenticando qualcuno) che in tutti questi anni hanno riempito pause pranzo, corridoi e fuori orario. Con voi ho imparato più giochi di carte che fisica, e ne è valsa assolutamente la pena.

Infine, grazie a tutte le persone che ho incontrato lungo questo percorso e che mi sono state vicine, anche solo con un messaggio, un caffè o una risata al momento giusto.

Grazie di tutto,
a tutti.

References

[1] R. Aliberti et al., "The anomalous magnetic moment of the muon in the standard model: An update," *Physics Reports*, vol. 1143, pp. 1–158, Nov. 2025, ISSN: 0370-1573. DOI: 10.1016/j.physrep.2025.08.002. [Online]. Available: http://dx.doi.org/10.1016/j.physrep.2025.08.002.

[2] G. Hall, U. Marconi, C. Matteuzzi, and D. Pocanic, "Proposal for phase 1 of the MUonE experiment," CERN, Geneva, Tech. Rep., 2024. [Online]. Available: https://cds.cern.ch/record/2896293.

[3] G. E. Uhlenbeck and S. Goudsmit, "Spinning electrons and the structure of spectra," *Nature*, vol. 117, pp. 264–265, 1926. DOI: 10.1038/117264a0. [Online]. Available: https://www.nature.com/articles/117264a0.

[4] P. A. M. Dirac, "The quantum theory of the electron," *Proceedings of the Royal Society of London. Series A*, vol. 117, no. 778, pp. 610–624, 1928. DOI: 10.1098/rspa.1928.0023.

[5] P. Kusch and H. M. Foley, "The magnetic moment of the electron," *Phys. Rev.*, vol. 74, pp. 250–263, 3 Aug. 1948. DOI: 10.1103/PhysRev.74.250. [Online]. Available: https://link.aps.org/doi/10.1103/PhysRev.74.250.

[6] J. Schwinger, "On quantum-electrodynamics and the magnetic moment of the electron," *Phys. Rev.*, vol. 73, pp. 416–417, 4 Feb. 1948. DOI: 10.1103/PhysRev.73.416. [Online]. Available: https://link.aps.org/doi/10.1103/PhysRev.73.416.

[7] X. Fan, T. G. Myers, B. A. D. Sukra, and G. Gabrielse, "Measurement of the electron magnetic moment," *Phys. Rev. Lett.*, vol. 130, p. 071 801, 7 Feb. 2023. DOI: 10.1103/PhysRevLett.130.071801. [Online]. Available: https://link.aps.org/doi/10.1103/PhysRevLett.130.071801.

[8] D. Hanneke, S. Fogwell, and G. Gabrielse, "New measurement of the electron magnetic moment and the fine structure constant," *Phys. Rev. Lett.*, vol. 100, p. 120 801, 12 Mar. 2008. DOI: 10.1103/PhysRevLett.100.120801. [Online]. Available: https://link.aps.org/doi/10.1103/PhysRevLett.100.120801.

[9] L. Morel, Z. Yao, P. Cladé, and S. Guellati-Khélifa, "Determination of the fine-structure constant with an accuracy of 81 parts per trillion," *Nature*, vol. 588, pp. 61–65, 2020. DOI: 10.1038/s41586-020-2964-7.

[10] R. H. Parker, C. Yu, W. Zhong, B. Estey, and H. Müller, "Measurement of the fine-structure constant as a test of the standard model," *Science*, vol. 360, no. 6385, pp. 191–195, 2018. DOI: 10.1126/science.aap7706.

[11] F. Jegerlehner, *The anomalous magnetic moment of the muon*. Springer, 2008, vol. 226.

[12] A. Keshavarzi, D. Nomura, and T. Teubner, "The muon g-2 and $\alpha(M_Z^2)$: A new data-based analysis," *Phys. Rev. D*, vol. 97, no. 11, p. 114 025, 2018. DOI: 10.1103/PhysRevD.97.114025. arXiv: 1802.02995 [hep-ph].

[13] F. Ambrosino et al., "Measurement of $\sigma(e^+e^- \to \pi^+\pi^-\gamma(\gamma))$ and the dipion contribution to the muon anomaly with the kloe detector," *Physics Letters B*, vol. 670, pp. 285–291, 2009. DOI: 10.1016/j.physletb.2008.10.060. arXiv: 0809.3950 [hep-ex].

[14] G. Venanzoni, "From hadronic cross section to the measurement of the vacuum polarization at kloe: A fascinating endeavour," *EPJ Web of Conferences*, vol. 166, p. 00 021, 2018. DOI: 10.1051/epjconf/201816600021.

[15] J. P. Lees et al., "Precise measurement of the $e^+e^- \to \pi^+\pi^-(\gamma)$ cross section with the initial-state radiation method at babar," *Phys. Rev. D*, vol. 86, p. 032 013, 3 Aug. 2012. DOI: 10.1103/PhysRevD.86.032013. [Online]. Available: https://link.aps.org/doi/10.1103/PhysRevD.86.032013.

[16] A. Anastasi, D. Babusci, et al., "Combination of kloe $\sigma(e^+e^- \to \pi^+\pi^-\gamma(\gamma))$ measurements and determination of $a_\mu^{\pi^+\pi^-}$ in the energy range $0.10 < s < 0.95$ GeV^2," *Journal of High Energy Physics*, vol. 2018, no. 3, p. 173, 2018. DOI: 10.1007/JHEP03(2018)173. arXiv: 1711.03085 [hep-ex].

[17] F. V. Ignatov et al., "Measurement of the $e^+e^- \to \pi^+\pi^-$ cross section from threshold to 1.2 gev with the cmd-3 detector," *Phys. Rev. D*, vol. 109, p. 112 002, 11 Jun. 2024. DOI: 10.1103/PhysRevD.109.112002. [Online]. Available: https://link.aps.org/doi/10.1103/PhysRevD.109.112002.

[18] T. Aoyama et al., "The anomalous magnetic moment of the muon in the standard model," *Physics Reports*, vol. 887, pp. 1–166, 2020. DOI: 10.1016/j.physrep.2020.07.006.

[19] M. Abe et al., "A new approach for measuring the muon anomalous magnetic moment and electric dipole moment," *Progress of Theoretical and Experimental Physics*, no. 5, p. 053C02, 2019. DOI: 10.1093/ptep/ptz030.

[20] MUonE Collaboration, *The m2 beam and its implications for muone*, CERN Indico, attachment: MuonE_coll_meeting_260319.pdf, 2019. [Online]. Available: https://indico.cern.ch/event/793576/contributions/3348762/attachments/1818102/2972443/MuonE_coll_meeting_260319.pdf.

[21] C. Carloni Calame, M. Passera, L. Trentadue, and G. Venanzoni, "A new approach to evaluate the leading hadronic corrections to the muon g-2," *Physics Letters B*, vol. 746, pp. 325–329, 2015, ISSN: 0370-2693. DOI: https://doi.org/10.1016/j.physletb.2015.05.020. [Online]. Available: https://www.sciencedirect.com/science/article/pii/S0370269315003573.

[22] K. Melnikov and A. Vainshtein, *Theory of the Muon Anomalous Magnetic Moment* (Springer Tracts in Modern Physics). Springer Berlin Heidelberg, 2006, vol. 216, ISBN: 978-3-540-32806-3. DOI: 10.1007/3-540-32807-6.

[23] G. Abbiendi, C. M. C. Calame, U. Marconi, G. Montagna, O. Nicrosini, and et al., "Measuring the leading hadronic contribution to the muon g-2 via μe scattering," *Eur. Phys. J. C*, vol. 77, no. 3, p. 139, 2017. DOI: 10.1140/epjc/s10052-017-4633-z. arXiv: 1609.08987 [hep-ex].

[24] R. N. Pilato, "The muone experiment: Mu-e elastic scattering as a key to understand the muon g-2 puzzle," in *Proceedings of The European Physical Society Conference on High Energy Physics — PoS(EPS-HEP2023)*, vol. 449, 2024, p. 305. DOI: 10.22323/1.449.0305.

[25] G. Abbiendi, "Letter of Intent: the MUonE project," CERN, Geneva, Tech. Rep., 2019, The collaboration has not yet a structure, therefore the names above are for the moment an indication of contacts. [Online]. Available: https://cds.cern.ch/record/2677471.

[26] M. Alacevich, C. M. C. Calame, M. Chiesa, G. Montagna, O. Nicrosini, and F. Piccinini, "Muon–electron scattering at nlo," *JHEP*, vol. 2019, no. 2, p. 155, 2019. DOI: 10.1007/JHEP02(2019)155. arXiv: 1811.06743 [hep-ph].

[27] M. Fael and M. Passera, "Muon–electron scattering at next-to-next-to-leading order," *Physical Review Letters*, vol. 122, p. 192 001, 2019. DOI: 10.1103/PhysRevLett.122.192001.

[28] "The Phase-2 Upgrade of the CMS Tracker," CERN, Geneva, Tech. Rep., 2017. DOI: 10.17181/CERN.QZ28.FLHW. [Online]. Available: https://cds.cern.ch/record/2272264.

[29] F. Zhang et al., "Prototyping and qualification of 2S modules for the CMS Outer Tracker upgrade at the HL-LHC," CERN, Geneva, Tech. Rep. 05, 2022. DOI: 10.1088/1748-0221/17/05/C05019. arXiv: 2112.01881. [Online]. Available: https://cds.cern.ch/record/2797707.

[30] R. N. Pilato, "Feasibility study of the muone experiment," Tutor: Prof. Graziano Venanzoni, Tesi di dottorato di ricerca, Università di Pisa, Pisa, Italia, Feb. 2023. [Online]. Available: https://etd.adm.unipi.it/t/etd-02222023-185026/.

[31] A. Arena, G. Cantatore, and M. Karuza, "Digital holographic interferometry for particle detector diagnostic," in *2022 45th Jubilee International Convention on Information, Communication and Electronic Technology (MIPRO)*, 2022, pp. 235–237. DOI: 10.23919/MIPRO55190.2022.9803636.

[32] A. Arena, *Muone experiment: Holographic alignment monitor for tracking detector modules*, 2022.

[33] P. Adzic and et al., "Energy resolution of the barrel of the cms electromagnetic calorimeter," *Journal of Instrumentation*, vol. 2, P04004, Apr. 2007. DOI: 10.1088/1748-0221/2/04/P04004. [Online]. Available: https://doi.org/10.1088/1748-0221/2/04/P04004.

[34] M. Raymond, J. Crooks, M. French, and G. Hall, "The mgpa electromagnetic calorimeter readout chip for cms," *IEEE Transactions on Nuclear Science*, vol. 52, no. 3, pp. 756–763, 2005. DOI: 10.1109/TNS.2005.850979.

[35] E. Spedicato and the MUonE Collaboration, "A prototype electromagnetic calorimeter for the muone experiment: Status and first performance results," *Journal of Instrumentation*, vol. 19, no. 02, p. C02044, 2024. DOI: 10.1088/1748-0221/19/02/C02044. [Online]. Available: https://iopscience.iop.org/article/10.1088/1748-0221/19/02/C02044.

[36] S. K. Kulis, "lpGBT Status and Plans," 2018. [Online]. Available: https://cds.cern.ch/record/2315489.

[37] A. Rose, "Serenity - An ATCA prototyping platform for CMS Phase-2," CERN, Geneva, Tech. Rep., 2019. DOI: 10.22323/1.343.0115. [Online]. Available: https://cds.cern.ch/record/2646388.

[38] AMD (formerly Xilinx), "Ultrascale+ fpgas — product tables and product selection guide," AMD, Tech. Rep. XMP103, Jul. 2025, Rev. 2.5. [Online]. Available: https://docs.amd.com/v/u/en-US/ultrascale-plus-fpga-product-selection-guide.

[39] P. Asenov et al., "A Geant4-based simulation study for a preliminary setup of the MUonE experiment," in *Proceedings of 41st International Conference on High Energy physics — PoS(ICHEP2022)*, vol. 414, 2022, p. 905. DOI: 10.22323/1.414.0905.

[40] M. Al-Turany et al., "The fairroot framework," *Journal of Physics: Conference Series*, vol. 396, p. 022 001, 2012. DOI: 10.1088/1742-6596/396/2/022001.

[41] Particle Data Group, "Passage of particles through matter," *Progress of Theoretical and Experimental Physics*, vol. 2023, no. 8, p. 083C01, 2023, See PDG Review, sec. "Multiple scattering". [Online]. Available: https://pdg.lbl.gov/2023/reviews/rpp2023-rev-passage-particles-matter.pdf.

[42] MUonE Collaboration, *Data preprocessor branch + muon filter reco*, CERN Indico slides, event 1563382, contribution 6591083, attachment 5484015, 2025. Accessed: Sep. 30, 2025. [Online]. Available: https://indico.cern.ch/event/1563382/contributions/6591083/attachments/3095643/5484015/Data%20Preprocessor%20branch%20+%20muon%20filter%20reco.pdf.

[43] CERN IT Monitoring, *Grafana — cern monit documentation*, CERN IT Monitoring Guide, Central Grafana instance (monit-grafana.cern.ch), access, roles, dashboard catalogue, 2025. [Online]. Available: https://monit.docs.cern.ch/grafana/.